

# Spectral anomalies and broken symmetries in maximally chaotic quantum maps

Laura Shou<sup>1,2\*</sup>, Amit Vikram<sup>3†</sup> and Victor Galitski<sup>3‡</sup>

**1** Condensed Matter Theory Center and Joint Quantum Institute, Department of Physics,  
University of Maryland, College Park, MD 20742, USA

**2** School of Mathematics, University of Minnesota, Minneapolis, MN 55455, USA

**3** Joint Quantum Institute and Department of Physics, University of Maryland, College Park,  
MD 20742, USA

\* [lshou@umd.edu](mailto:lshou@umd.edu), † [amitv@umd.edu](mailto:amitv@umd.edu), ‡ [galitski@umd.edu](mailto:galitski@umd.edu)

## Abstract

Spectral statistics such as the level spacing statistics and spectral form factor (SFF) are widely expected to accurately identify “ergodicity,” including the presence of underlying macroscopic symmetries, in generic quantum systems ranging from quantized chaotic maps to interacting many-body systems. By studying various quantizations of maximally chaotic maps that break a discrete classical symmetry upon quantization, we demonstrate that this approach can be misleading and fail to detect macroscopic symmetries. Notably, the same classical map can exhibit signatures of different random matrix symmetry classes in short-range spectral statistics depending on the quantization. While the long-range spectral statistics encoded in the early time ramp of the SFF are more robust and correctly identify macroscopic symmetries in several common quantizations, we also demonstrate analytically and numerically that the presence of Berry-like phases in the quantization leads to spectral anomalies, which break this correspondence. Finally, we provide numerical evidence that long-range spectral rigidity remains directly correlated with ergodicity in the quantum dynamical sense of visiting a complete orthonormal basis.

Copyright attribution to authors.

This work is a submission to SciPost Physics.

License information to appear upon publication.

Publication information to appear upon publication.

Received Date

Accepted Date

Published Date

1

## 2 Contents

3	<b>1 Introduction</b>	2
4	1.1 Background and motivation	2
5	1.2 Summary of this paper	3
6	<b>2 Models</b>	4
7	<b>3 Overview of results</b>	7
8	3.1 Nearest-neighbor level spacing statistics	7
9	3.2 Spectral form factor	8
10	3.3 Periodic orbit expansion	11

11	3.4 Symmetry breaking and quantum dynamical ergodicity	14
12	<b>4 Operator symmetries and level spacing statistics</b>	<b>17</b>
13	4.1 Operator symmetries	17
14	4.2 Level spacing statistics	18
15	4.3 Approximate symmetry classes for the Balazs–Voros quantization	19
16	<b>5 Spectral form factor analysis</b>	<b>21</b>
17	<b>6 Semiclassical trace formula</b>	<b>23</b>
18	6.1 Classical dynamics revisited	23
19	6.2 Periodic orbit theory for the Generic quantizations	24
20	6.3 Periodic orbit theory for the Shor baker quantizations	25
21	<b>7 Conclusion</b>	<b>28</b>
22	<b>A Reflection commutators</b>	<b>29</b>
23	<b>B Commutator for approximate symmetry</b>	<b>29</b>
24	<b>C Details for the computation of the early time SFF slope</b>	<b>31</b>
25	<b>D Shor baker matrix stationary phase approximation</b>	<b>31</b>
26	<b>References</b>	<b>33</b>

---

28

## 29 1 Introduction

### 30 1.1 Background and motivation

31 The connection between the statistics of energy levels and a variety of ergodic phenomena  
 32 is a foundational problem in the study of quantum signatures of chaos [1] and the statisti-  
 33 cal mechanics of quantum many-body systems [2]. In *generic* systems with a classical limit  
 34 or many-body structure, an empirically successful approach has been to look for signatures  
 35 of eigenvalue statistics associated with random matrix theory (RMT) [3], in order to diag-  
 36 nose “ergodicity” if these are present [4–20], and infer its absence otherwise [21–26]; indeed,  
 37 the presence of “ideal” RMT statistics can be shown to be sufficient (but not necessary) for  
 38 an ergodic exploration of an orthonormal basis in the Hilbert space of a general quantum  
 39 system [27]. However, for a complete understanding of the utility of eigenvalue statistics,  
 40 it is essential to quantitatively characterize deviations from this idealized behavior, particu-  
 41 larly to identify where such statistics no longer accurately diagnose different forms of ergod-  
 42 icity/thermalization.

43 There are a number of interesting systems where deviations from RMT have been observed  
 44 that point to an increasing need to characterize non-RMT behavior [21, 27–35]. Barring spe-  
 45 cific cases with alternate explanations, these deviations are generally due to *emergent* quantum  
 46 symmetries not present in the classical system [1], usually connected to the classical periodic  
 47 orbits, that lead to ergodicity-breaking after the Ehrenfest time [36, 37] at which classical and  
 48 quantum evolutions diverge significantly. Prominent examples include the modular multipli-

49 cation [30, 38, 39] and cat maps [28, 29] (which become exactly periodic in their standard  
 50 quantization), and chaotic dynamics on arithmetic domains in hyperbolic surfaces [32, 33],  
 51 where RMT statistics are present only if specific boundary conditions are imposed on quanti-  
 52 zation [34], being strongly violated by emergent Hecke symmetries [32] otherwise.

53 In this work, we identify and characterize anomalies in spectral statistics of a different  
 54 (and essentially opposite) nature to the above systems, originating in the quantum mechani-  
 55 cal breaking of *discrete* symmetries that are rigorously present at the macroscopic scale. The  
 56 existence and relevance of such anomalies is suggested, for instance, by studies of certain  
 57 exceptional billiard systems [40–43]. Specifically, we consider quantizations of maximally  
 58 chaotic quantum maps in which we show that discrete macroscopic symmetries are *not* accu-  
 59 rately reflected in the most commonly used measures of spectral statistics: (1) the spectral  
 60 form factor (SFF) [1, 9], which measures spectral rigidity over different energy scales as a  
 61 function of time (namely, long-range at early times, and short-range at late times), (2) the  
 62 (short-range) nearest neighbor level spacing statistics [1, 4–7], and (3) the adjacent gap ra-  
 63 tios [44] (characterizing the short-range next-nearest-neighbor statistics). The short-range  
 64 statistics in particular show especially stark violations. These violations are striking in the  
 65 context of the use of spectral statistics to *identify* discrete symmetries of the time evolution  
 66 operator. While such diagnostics are effective in a variety of systems exhibiting block RMT be-  
 67 havior [10, 45–48], our results show they cannot always be relied upon, even in simple systems  
 68 with a well-defined classical limit.

## 69 1.2 Summary of this paper

70 We aim to illustrate the unreliability of common spectral statistics in identifying discrete sym-  
 71 metries as may be present in quantized chaotic maps or many-body systems. To ensure that  
 72 the systems being compared have an identical and well-understood macroscopic behavior, we  
 73 consider classical maps that are *known* to have two discrete symmetries that square to unity  
 74 (i.e., restore the original system on acting twice). More specifically, we study spectral statistics  
 75 in different quantizations [49, 50] of the *A*-baker’s maps, which are classically paradigmatic  
 76 examples of ergodicity with maximally chaotic (Bernoulli) behavior [51]. Incidentally, in ad-  
 77 dition to having a classical limit, these quantizations are particularly amenable to implemen-  
 78 tation as many-body Floquet quantum circuits [52, 53]. Further, all these quantizations reduce  
 79 in the classical limit to the same classical *A*-baker’s maps, and thus possess the same two dis-  
 80 crete symmetries (Sec. 2). These are: a canonical reflection symmetry, and an anticanonical  
 81 time-reversal symmetry, which respectively correspond to a unitary reflection and antiunitary  
 82 time-reversal operator on quantization.

83 Our main qualitative results, described more thoroughly in Sec. 3, are as follows. While  
 84 the spectral statistics of some of these quantizations are already known to be “unusual”, a key  
 85 observation in this work is that these unusual features can be satisfactorily organized in terms  
 86 of a simple, and potentially generalizable, picture of different levels of “discrete symmetry  
 87 breaking” in the spectral statistics. These anomalies are to be evaluated relative to the follow-  
 88 ing general expectation based on RMT [1, 3]: the presence and absence of the time-reversal  
 89 symmetry respectively correspond to COE and CUE level statistics, with the presence or ab-  
 90 sence of the reflection symmetry indicating a 2-block or 1-block structure of the associated  
 91 random matrix. In particular, based on their classical symmetries, quantized *A*-baker’s maps  
 92 would be expected to have the spectral statistics of 2-block COE. With this context, we identify  
 93 spectral anomalies of two types (Sec. 3.1, 3.2):

- 94 1. “Weak anomalies” whose primary effect is in the regime of long times corresponding to  
 95 short-range energy spacings, leading to full (single-block) RMT-like behavior in the mean  
 96 gap ratio statistic and nearest neighbor level spacings for large  $A$  (ranging from 1-block

97 COE to CUE). However, the early-time SFF is consistent with the presence of the unitary  
 98 reflection symmetry (2-block COE). These demonstrate that short-range measures can  
 99 be misleading indicators of discrete symmetries.

100 2. “Strong anomalies” that affect even the regime of early times and long-range energy  
 101 spacings in addition to the long-time regime as above, where even the early-time SFF  
 102 shows RMT behavior consistent with the absence of unitary symmetries (1-block COE).  
 103 These show that even long-range measures can be misleading in certain circumstances.

104 Subsequently, we study the connection between these spectral anomalies and dynamics.  
 105 We show analytically and numerically that strong anomalies emerge from the inclusion of ad-  
 106 ditional phases in specific quantizations [49], which have no impact in the classical limit, but  
 107 occur as Berry-like phases in the semiclassical periodic orbit expression (Sec. 3.3). Further, we  
 108 numerically study quantum dynamics in the Hilbert space in the sense of cyclic ergodicity [27],  
 109 and find that strong anomalies appear to induce cyclic ergodicity where weak anomalies do  
 110 not, verifying the direct connection between long-range spectral statistics and ergodic quan-  
 111 tum dynamics irrespective of classical symmetries (Sec. 3.4). The remaining sections offer  
 112 additional analytical and numerical details concerning these results.

## 113 2 Models

114 In this section, we introduce the classical and quantum systems.

115 *Classical maps*— The classical maps we consider are the  $A$ -baker’s maps [49, 51, 54], which  
 116 act on the 2-torus  $\mathbb{T}^2 = \mathbb{R}^2/\mathbb{Z}^2$  (identified with the unit square) via

$$(q, p) \mapsto \left( Aq - [Aq], \frac{p + [Aq]}{A} \right), \quad (1)$$

117 for  $(q, p) \in [0, 1) \times [0, 1)$  and  $A \geq 2$  an integer. When  $A = 2$ , this is the same as the usual  
 118 baker’s map. We depict the action of the  $A$ -baker’s map for  $A = 3$  on the unit square in Fig. 1.

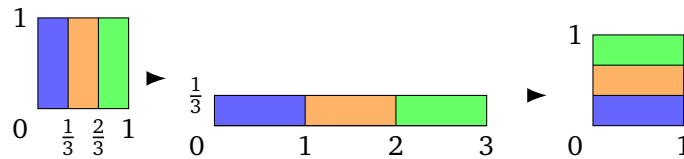


Figure 1: Visualization of the action of the 3-baker’s map, starting from the left unit square and ending with the right unit square. The intermediate step shows the stretching, cutting, and stacking operation described by Eq. (1).

119 The classical  $A$ -baker’s map is equivalent to a 2-sided Bernoulli shift [49, 51, 55] and is  
 120 thus maximally chaotic. It represents a fairly “universal” model of chaotic dynamics, as any  
 121 K-mixing (ergodic and chaotic) system with sufficiently large Kolmogorov-Sinai entropy [56]  
 122 (essentially the sum of nonnegative Lyapunov exponents)  $h \geq \ln A$  can be coarse-grained into  
 123 a given  $A$ -baker’s map (or most directly, the corresponding Bernoulli shift), by the Sinai factor  
 124 theorem [57, 58]. The  $A$ -baker’s maps possess two symmetries, a time-reversal (TR) symmetry  
 125  $T : (q, p) \mapsto (p, q)$  and a reflection symmetry

$$R : (q, p) \mapsto (1 - q, 1 - p), \quad (2)$$

126 which will play key roles in our analysis. Due to the time-reversal symmetry, one expects  
 127 the RMT symmetry class for the corresponding quantized systems to be that of the circular

128 orthogonal ensemble (COE). Additionally, due to the reflection symmetry, one expects two  
 129 distinct COE symmetry classes, leading to an overall behavior resembling a direct sum of two  
 130 COE matrices. As we will demonstrate, however, these general expectations need not hold  
 131 even approximately when the classical symmetries are broken upon quantization.

132 We briefly note that while we do not exhaustively verify the absence of any further classical  
 133 symmetries for  $A > 2$ , numerical results counting values of the classical action on orbits (as  
 134 defined in Eq. (30)) suggest the above symmetries are likely the only two. In any case however,  
 135 the main conclusions of this paper that spectral statistics can fail to detect symmetries would  
 136 still hold.

137 *Balazs–Voros, Saraceno, and generic quasiperiodic quantizations*— For quantizing a map like  
 138 the classical  $A$ -baker’s map Eq. (1), there is no unique method; essentially one just requires  
 139 the associated quantum map to be a unitary  $N \times N$  matrix that reduces to the classical map in  
 140 the semiclassical limit  $N \rightarrow \infty$ . The first quantization of the baker’s map was given by Balazs  
 141 and Voros in [49]; for the simplest case  $A = 2$  and  $N$  even, this reads

$$\hat{B}_N = \hat{F}_N^{-1} \begin{pmatrix} \hat{F}_{N/2} & \mathbf{0} \\ \mathbf{0} & \hat{F}_{N/2} \end{pmatrix}, \quad (3)$$

142 where  $\hat{F}_N$  is the  $N \times N$  discrete Fourier transform (DFT) matrix defined via

$$(\hat{F}_N)_{jk} = \frac{1}{\sqrt{N}} e^{-2\pi i jk/N}, \quad j, k = 0, \dots, N-1.$$

143 This quantization using the standard DFT matrix is associated with periodic boundary con-  
 144 ditions on the torus  $\mathbb{T}^2$ . In order to study different quantum symmetries, we will consider  
 145 the natural “generic” quantization for the  $A$ -baker’s map with quasiperiodic boundary condi-  
 146 tions [49, 50, 59] corresponding to  $\theta = (\theta_1, \theta_2) \in [0, 1]^2$ ,

$$\text{Gen}_{A,N}^{\theta_1, \theta_2} = (\hat{F}_N^{\theta_1, \theta_2})^{-1} \bigoplus_{j=0}^{A-1} \hat{F}_{N/A}^{\theta_1, \theta_2}, \quad (4)$$

147 where

$$(\hat{F}_N^{\theta_1, \theta_2})_{jk} = \frac{1}{\sqrt{N}} e^{-2\pi i (j+\theta_1)(k+\theta_2)/N} \quad (5)$$

148 is a generalized DFT matrix, and  $N \in AN$ . The direct sum part of Eq. (4) produces a block  
 149 diagonal matrix consisting of generalized DFT matrices  $\hat{F}_{N/A}^{\theta_1, \theta_2}$ .

150 The case  $\theta_1 = \theta_2 = 0$  is the Balazs–Voros quantization of the  $A$ -baker’s map, for which we  
 151 may use the abbreviated label “BV” in plots or tables. The Balazs–Voros quantizations preserve  
 152 an operator TR symmetry but break an operator reflection symmetry (Sec. 4.1), and for  $A = 2$   
 153 were observed to show anomalous level spacings behavior depending on the dimension  $N$  [49].

154 The case  $\theta_1 = \theta_2 = 1/2$  is the Saraceno quantization from [50], and corresponds to an-  
 155 tiperiodic boundary conditions. This quantization preserves TR symmetry and moreover pre-  
 156 serves the classical reflection symmetry, as it commutes with the microscopic reflection opera-  
 157 tor  $R_N : |x\rangle \mapsto |N-x-1\rangle$ . As a consequence, this was observed for  $A = 2$  to restore COE level  
 158 spacing statistics within each symmetry class.

159 In general, for  $\theta_1 \neq \theta_2$ , the generic quantization in Eq. (4) does not appear to preserve a  
 160 clear operator TR or reflection symmetry like in the Saraceno case. Possible symmetries are  
 161 discussed further in Sec. 4.1 and Appendix A.

162 *Shor baker quantization*— In addition to the above generic (quasi)periodic quantizations,  
 163 we consider the “Shor baker quantizations” from [38, 39]. These quantizations are part of the

164 quantum baker’s map decomposition of the modular multiplication operator in Shor’s factoring  
 165 algorithm [30], and can be defined as

$$\hat{S}_{A,N} = \hat{F}_N^{-1} \left( \bigoplus_{j=0}^{A-1} e^{2\pi i j^2/A} \hat{F}_{N/A}^{0,-j/A} \right), \quad (6)$$

166 where  $F_{N/A}^{0,-j/A}$  denotes a generalized DFT matrix defined via Eq. (5). These Shor baker quan-  
 167 tizations again appear to break both the operator TR and reflection symmetries.

168 *Phase variants*— Finally, we consider “phase variant quantizations” by adding arbitrary  
 169 Berry-like phases  $e^{2\pi i \alpha} = (e^{2\pi i \alpha_0}, \dots, e^{2\pi i \alpha_{A-1}})$  to the DFT block sectors of the previous  $A$ -baker’s  
 170 map quantizations. These are written in the right column of Tab. 1. These quantizations have  
 171 historically been considered as variations on the usual Balazs–Voros or Saraceno quantizations  
 172 since [49], but generally are overlooked in favor of the simpler standard/phaseless quantiza-  
 173 tions. For generic or random phases, we will see that the phase variant quantizations exhibit  
 174 significantly different spectral statistics than their corresponding standard/phaseless quanti-  
 175 zations.

	Standard/Phaseless	Phase variant
Balazs–Voros	$\hat{F}_N^{-1} \bigoplus_{j=0}^{A-1} \hat{F}_{N/A}$	$\hat{F}_N^{-1} \bigoplus_{j=0}^{A-1} e^{2\pi i \alpha_j} \hat{F}_{N/A}$
Saraceno	$\left(\hat{F}_N^{\frac{1}{2}, \frac{1}{2}}\right)^{-1} \bigoplus_{j=0}^{A-1} \hat{F}_{N/A}^{\frac{1}{2}, \frac{1}{2}}$	$\left(\hat{F}_N^{\frac{1}{2}, \frac{1}{2}}\right)^{-1} \bigoplus_{j=0}^{A-1} e^{2\pi i \alpha_j} \hat{F}_{N/A}^{\frac{1}{2}, \frac{1}{2}}$
Generic Gen $_A^{\theta_1, \theta_2}$	$\left(\hat{F}_N^{\theta_1, \theta_2}\right)^{-1} \bigoplus_{j=0}^{A-1} \hat{F}_{N/A}^{\theta_1, \theta_2}$	$\left(\hat{F}_N^{\theta_1, \theta_2}\right)^{-1} \bigoplus_{j=0}^{A-1} e^{2\pi i \alpha_j} \hat{F}_{N/A}^{\theta_1, \theta_2}$
Shor baker	$\hat{F}_N^{-1} \bigoplus_{j=0}^{A-1} e^{2\pi i j^2/A} \hat{F}_{N/A}^{0, -j/A}$	$\hat{F}_N^{-1} \bigoplus_{j=0}^{A-1} e^{2\pi i \alpha_j} \hat{F}_{N/A}^{0, -j/A}$

Table 1: Definitions of the different quantizations of the  $A$ -baker’s map. Balazs–Voros is the same as Gen $_A^{0,0}$ , and Saraceno the same as Gen $_A^{1/2,1/2}$ . The “default” quantizations will be the standard/phaseless ones, and we may simply refer to them as the “Balazs–Voros/Saraceno/Generic/Shor baker” quantizations, while for the quantizations with arbitrary phases  $e^{2\pi i \alpha}$  we will always specify that it involves the extra phases.

176 All of the quantizations in Tab. 1 are quantizations of the classical  $A$ -baker’s map in the  
 177 sense that they map coherent states localized in phase space near  $(q, p)$ , to coherent states  
 178 localized in phase space near the classical time-evolved point  $(Aq - [Aq], \frac{p+[Aq]}{A})$  as  $N \rightarrow \infty$ .  
 179 For details, see [60, §4] and [39, Suppl. Mat.], noting that for quasiperiodic boundary con-  
 180 ditions one must use the appropriate quasiperiodic coherent states and generalized DFT ma-  
 181 trix  $\hat{F}_N^{\theta_1, \theta_2}$ . Additionally, for the Balazs–Voros (and Saraceno) quantizations, the argument  
 182 in [60, §5] proves a rigorous “Egorov property” concerning time-evolution of quantum observ-  
 183 ables  $\text{Op}_N(a)$  corresponding to classical observables  $a$  on  $\mathbb{T}^2$  supported away from classical  
 184 discontinuities,

$$\|\hat{U}_N^t \text{Op}_N(a) \hat{U}_N^{-t} - \text{Op}_N(a \circ B^{-t})\| \xrightarrow{N \rightarrow \infty} 0, \quad (7)$$

185 where  $\hat{U}_N$  is the quantization and  $B$  is the classical  $A$ -baker’s map. The argument is insensi-  
 186 tive to phases on the DFT blocks, so that the same rigorous correspondence holds for their  
 187 corresponding phase variant quantizations. We expect the same argument (with some minor  
 188 adaptations) applies to the generic quasiperiodic and Shor baker quantizations both with and  
 189 without phases.



### 190 3 Overview of results

191 In this section, we explain the main results summarized in Tab. 2, which compares the nearest-  
 192 neighbor level spacing statistics and spectral form factor behavior by quantization and presence  
 193 of quantum symmetries. We provide the numerical results for the level spacing statistics, and  
 194 both analytical and numerical results for the early time SFF slope. Due to the classical TR  
 195 and reflection symmetries of the classical  $A$ -baker’s map, one would expect its quantizations  
 196 to exhibit spectral statistics similar to a 2-block COE matrix (a direct sum of two independent,  
 197 equal sized COE matrices). As has been well-known since [49], this already does not hold  
 198 for the level spacing statistics of the Balazs–Voros quantization with  $A = 2$ , which display  
 199 intermediate level spacing statistics due to the mixing of symmetry sectors. But as we will see,  
 200 there are several subtleties involved with the spectral statistics, and the results will depend  
 201 on both the spectral statistic chosen and the particular quantization type. We emphasize the  
 202 following main points.

- 203 (A) Unlike the  $A = 2$  case, for large  $A$ , the level spacing statistics actually do appear to follow  
 204 classical RMT behavior for all considered quantizations. However, this RMT behavior can  
 205 be of the wrong symmetry class (e.g. CUE vs COE) and/or reflect the wrong number of  
 206 symmetry sectors.
- 207 (B) For the standard/phaseless quantizations, the early time SFF behavior correctly identi-  
 208 fies the RMT symmetry class and symmetry sectors, even as the level spacings do not.  
 209 This provides a resolution for the non-RMT level spacing statistics in [49], as well as for  
 210 the wrong symmetry class behavior in the aforementioned point. Such spectral anoma-  
 211 lies, where the long-range statistics remain reliable even as the short-range ones do not,  
 212 are those we term “weak anomalies”, and they appear to be well-described by a *block*  
 213 Rosenzweig–Porter-like interpolation between RMT ensembles.
- 214 (C) The Berry-like phases in the phase variant quantizations produce “strong spectral anoma-  
 215 lies”, where even the early time SFF misses one of the classical symmetries. Using a  
 216 semiclassical periodic orbit analysis, we analytically characterize the early time SFF slope  
 217 as a function of the phase choices, and show a generic choice of phases (probability 1  
 218 set) will always lead to strong anomalies. We note that the reflection and TR symmetries  
 219 continue to emerge in the classical limit despite these phases.
- 220 (D) The presence of strong anomalies is verified numerically to be tied to ergodicity in a  
 221 quantum dynamical sense of exploring an orthonormal basis in the Hilbert space [27],  
 222 irrespective of symmetries in the classical limit. However, weak anomalies do not appear  
 223 to be sufficiently strong to induce ergodic dynamics in this sense.

#### 224 3.1 Nearest-neighbor level spacing statistics

225 While RMT level spacing statistics are commonly used as an indicator (or even definition)  
 226 of “quantum chaotic” systems [1], the  $A$ -baker’s map quantizations can exhibit non-universal  
 227 level spacing statistics that are strongly sensitive to the particular quantization choice. The  
 228 first hint of complication is that the Balazs–Voros quantization in Eq. (3) ( $A = 2$ ) was observed  
 229 in [49] to have level spacing statistics that vary depending on  $N$ ; they almost never look COE  
 230 or block COE, which was explained as due to the quantization breaking the classical reflection  
 231 symmetry in Eq. (2) and mixing symmetry sectors together.

232 Surprisingly, as demonstrated by Figs. 2 and 3, we find the level spacing statistics and mean  
 233 gap ratio statistic (computed from the level spacings [44, 48, 61]) for the higher slope  $A$ -baker’s  
 234 maps begin to look very close to those of a single COE or CUE matrix as  $A$  increases, for all

		BV	Saraceno	$\text{Gen}_A^{\theta_1, \theta_2}$	Shor baker
$A = 2$	Level spacings	mixed	2-COE	2-COE/mixed	mixed
	SFF slope	4	4	4	4
$A$ large	Level spacings	COE	2-COE	CUE	CUE
	SFF slope	4	4	4	4
		$\text{BV}(\alpha)$	$\text{Saraceno}(\alpha)$	$\text{Gen}_A^{\theta_1, \theta_2}(\alpha)$	$\text{Shor baker}(\alpha)$
$A = 2$	Level spacings	COE	COE	COE/mixed	mixed
	SFF slope	2	2	2	2
$A$ large	Level spacings	COE	COE	CUE	CUE
	SFF slope	2	2	2	2

Table 2: Summary of spectral statistics for the various quantizations of the  $A$ -baker’s map, with the standard or phaseless quantizations in the top section, and the random phase variant quantizations in the bottom section. The columns for the generic quantization  $\text{Gen}_A^{\theta_1, \theta_2}$  and its phase quantization reflect the choices  $\theta = (0.2, 0.7)$  and  $(0, 0.5)$  for numerics, though the SFF slope behavior we derive through the periodic orbit analysis applies to any choice of  $\theta$ . As seen in the table, the level spacing statistics (and mean gap ratio) vary greatly across all quantizations, and only accurately reflect the classical symmetry sectors over all  $A$  for the standard Saraceno quantization, which preserves both classical symmetries upon quantization. The early time SFF slope successfully identifies the symmetry sectors for all standard/phaseless quantizations (top section), even when the operator does not exhibit a clear analogue of the classical symmetries. However, the SFF misses the reflection symmetry in the random phase variant quantizations in the bottom section. The entries labeled “mixed” indicate level spacings that do not adhere to a single RMT or block-RMT ensemble, and instead look somewhere inbetween ensembles.

235 quantizations except the standard Saraceno quantization. Thus for large values of  $A$ , these  
 236 level spacing statistics appear RMT, but reflect the *wrong* symmetry classes. The effect of the  
 237 classical reflection symmetry appears to completely disappear for large  $A$  (for non-Saraceno  
 238 quantizations), and for some quantizations the TR symmetry separating COE from CUE is  
 239 ignored as well. For reference, the mean gap ratio values for the RMT ensembles as derived  
 240 in [48, 61] are provided in Tab. 3.

241 Although all quantizations share the classical limit of an  $A$ -baker’s map, they exhibit a  
 242 wide variety of level spacing and gap ratio statistics, ranging from the expected 2-block COE  
 243 behavior, to single block COE, to single block CUE, and to intermediate or mixed statistics  
 244 inbetween two RMT ensembles. We observe that for large  $A$ , it appears these short-range  
 245 spectral statistics reflect certain symmetries of the quantized operator (Sec. 4.1, Appendix A),  
 246 but not necessarily those of the underlying classical map.

### 247 3.2 Spectral form factor

248 The spectral form factor (SFF) is the Fourier transform of the 2-point level correlation func-  
 249 tion [1, 3]. For  $\hat{U}_N$  an  $N \times N$  unitary matrix, the SFF is given by the formula

$$\text{SFF}(t) = \frac{1}{N} |\text{Tr}(\hat{U}_N^t)|^2 = \frac{1}{N} \sum_{j,k=1}^N e^{it(\theta_j - \theta_k)}, \quad (8)$$

250 where  $(\theta_j)_{j=1}^N$  are the eigenangles of  $\hat{U}_N$ . The normalization is chosen so that the SFF can be  
 251 conveniently analyzed and compared across different values of  $N$ . For early times  $t > 0$ , the



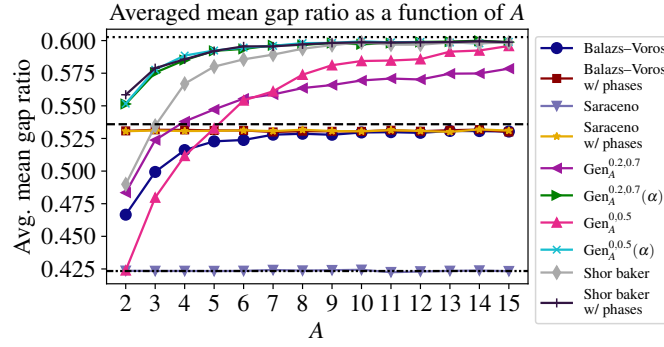


Figure 2: Averaged mean gap ratio for quantizations of the  $A$ -baker’s map, as a function of  $A$ . Each point represents an average over 50 values of  $N \in \mathbb{A}\mathbb{N}$ , starting near  $N = 5000$ . The horizontal lines, from top to bottom, plot the RMT reference values for CUE (dotted), COE (dashed), and 2-block COE (dash-dot-dotted). Only the standard Saraceno quantizations (downward triangle) exhibit mean gap ratios close to the expected 2-block COE value for all  $A$ .

252 SFF measures long-range spectral correlations, while for larger times  $t$ , the SFF describes finer  
 253 spectral correlations such as level spacings and eventually discreteness of the spectrum.

254 Letting  $\tau = t/N$ , there is the well-known formula for the COE form factor averaged over the  
 255 random ensemble in the limit  $N \rightarrow \infty$  [1], which for early times  $\tau$  yields  $\langle \text{SFF}_{\text{COE}}(\tau) \rangle = 2\tau + \mathcal{O}(\tau^2)$ .  
 256 For 2-block COE matrices, the corresponding ensemble-averaged SFF is  $\langle \text{SFF}_{2\text{-COE}}(\tau) \rangle = \langle \text{SFF}_{\text{COE}}(2\tau) \rangle$ .  
 257 Thus the early time SFF slope is 2 for a single COE matrix, and 4 for the 2-block COE matrix.  
 258 For the  $A$ -baker’s map quantizations, since we do not have an ensemble of matrices to average  
 259 over, we average the SFF by averaging over neighboring points as described in Appendix C.

260 We first demonstrate that the early time (averaged) SFF resolves the two issues with the  
 261 level spacing statistics for the standard/phaseless quantizations, (i) the non-universal behavior  
 262 for small  $A$  of the Balazs–Voros/Generic/Shor baker quantizations, and (ii) the apparent dis-  
 263 appearance of two distinct symmetry sectors for the same quantizations with larger  $A$ . These  
 264 cases thus correspond to “weak anomalies”, for which the SFF provides a satisfactory diagnos-  
 265 tic of the spectral behavior and classical symmetries.

266 As shown in the top row of Fig. 4, for very early times  $\tau$ , the SFFs for the standard phase-  
 267 less quantizations follow the slope 4 reference SFF behavior for the 2-block COE, correctly  
 268 reflecting the classical map symmetries. The longer time behaviors (corresponding to shorter  
 269 range statistics) however vary greatly. For larger  $\tau$ , the Saraceno quantizations (and  $\text{Gen}_{A=2}^{0,0.5}$ )  
 270 continue to follow the 2-block COE SFF, as previously demonstrated for the Saraceno  $A = 2$   
 271 quantization in [62], but the other standard quantizations appear to cross over to the single  
 272 COE or CUE SFF at a time  $\tau$  that decreases as  $A$  increases. Since the level spacing statis-  
 273 tics are short-range, corresponding to larger  $\tau$ , this faster cross-over explains the Balazs–  
 274 Voros/Generic/Shor baker matrix level spacing histograms approaching those of a single COE  
 275 or CUE matrix as  $A$  increases. For these cases, which describe “weak anomalies”, both the  
 276 RMT nature and symmetry sectors are readily apparent in the SFF, in contrast to the differing  
 277 information from the level spacing statistics.

278 The phase variant quantizations hold the surprise however. As shown in the bottom row of  
 279 Fig. 4, the addition of random phases to the quantizations interferes with the classical reflection  
 280 symmetry in a way that the early time SFF fails to detect it. Instead, the early time averaged  
 281 SFF has slope 2, capturing only the classical TR symmetry. (The level spacings are of even less  
 282 help, as seen in Figs. 2 and 3). We remark that from Fig. 4, it is not entirely clear whether it is  
 283 the TR or reflection symmetry that is missed by the early time SFF; the SFF for several of the

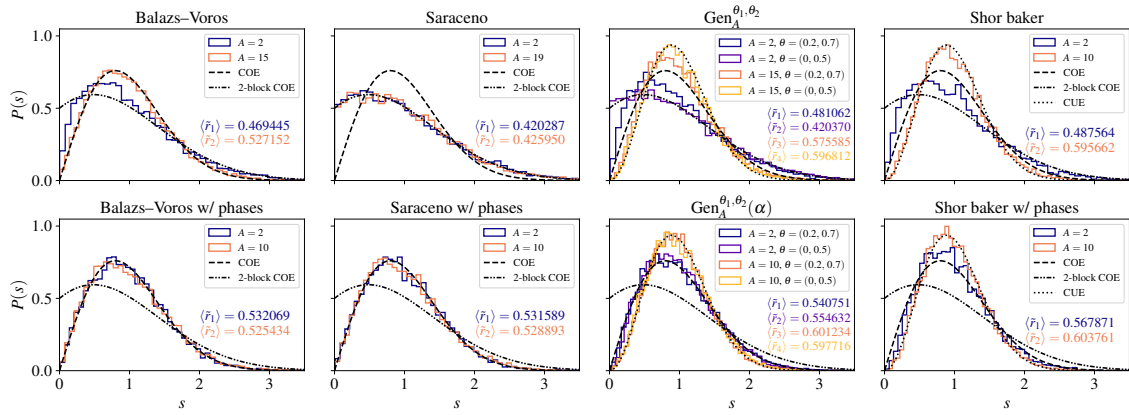


Figure 3: Level spacing histograms for the different quantizations of the  $A$ -baker’s map, for  $N = 9690$ . Note the variety of behaviors—COE, 2-block COE, mixed/indeterminate, and even CUE—that can arise, despite the same classical map symmetries. Only the phaseless Saraceno quantizations and phaseless  $\text{Gen}_{A=2}^{0,0.5}$  quantization appear to follow the 2-block COE curve. The mean gap ratio statistic  $\langle \bar{r} \rangle$  is also computed for each quantization.

284 quantizations follows the COE curve which strongly suggests it is the reflection symmetry that  
 285 is broken in those cases, but the SFF for other quantizations crosses over to the CUE curve.  
 286 From the periodic orbit analysis below, we will see that it is still the reflection symmetry that  
 287 is broken at early times in all cases. From the periodic orbit analysis, we will also be able  
 288 to identify the specific phases  $\alpha$  that produce an SFF slope of 4, which is a measure zero set  
 289 but contains more elements than just those corresponding to the standard/phaseless ( $\alpha_j = 0$ )  
 290 quantizations.

291 In addition to the SFF plots in Fig. 4, we plot the best fit SFF slope over a wide range  
 292 of dimensions  $N$  in Fig. 5. Unlike the standard/phaseless quantizations which produce SFFs  
 293 with slope near 4 that accurately describe the classical symmetry sectors, the quantizations  
 294 with random phases produce SFFs with slope near 2, thereby hiding the classical  $R$  symmetry.

295 Overall, as summarized in Tab. 2, although the early time SFF slope correctly identifies both  
 296 classical symmetries for the standard/phaseless quantizations (“weak anomalies”), it only cap-  
 297 tures one classical symmetry for the phase variant quantizations (“strong anomalies”). Mean-  
 298 while the level spacings fare worse, missing either one or both classical symmetries in almost  
 299 all quantizations.

300 Based on the level spacings and SFF behaviors, we find it appears that the spectral statistics  
 301 for these quantized  $A$ -baker’s maps look like those of a Rosenzweig–Porter-like [45] interpo-  
 302 lation between a 2-block COE matrix and a standard CUE or COE matrix (for standard quan-  
 303 tizations), or between a COE matrix and a CUE matrix (for phase variant quantizations). For  
 304 the former case, this type of *block* Rosenzweig–Porter model was introduced (for block GUE)  
 305 in [26] as a model for glassy behavior. In our case with unitary matrices, we will utilize a  
 306 different interpolation to preserve unitarity, namely a geodesic path between unitary matrices  
 307  $U_0$  and  $U_1$  given by

$$f(t) = U_0 \exp(t \log(U_0^\dagger U_1)), \quad (9)$$

308 for  $0 \leq t \leq 1$ . For interpolating between a 2-block COE matrix  $U_0$  and a COE matrix  $U_1$ , we  
 309 write  $U_0 = V^T V$  and  $U_1 = W^T W$  for unitaries  $V$  and  $W$ , apply Eq. (9) to obtain an interpolation  
 310  $f_{VW}(t)$  between  $V$  and  $W$ , and then take the interpolation  $F(t) = f_{VW}(t)^T f_{VW}(t)$  between  $U_0$   
 311 and  $U_1$ . In the other two cases, interpolating between 2-block COE and CUE or between COE

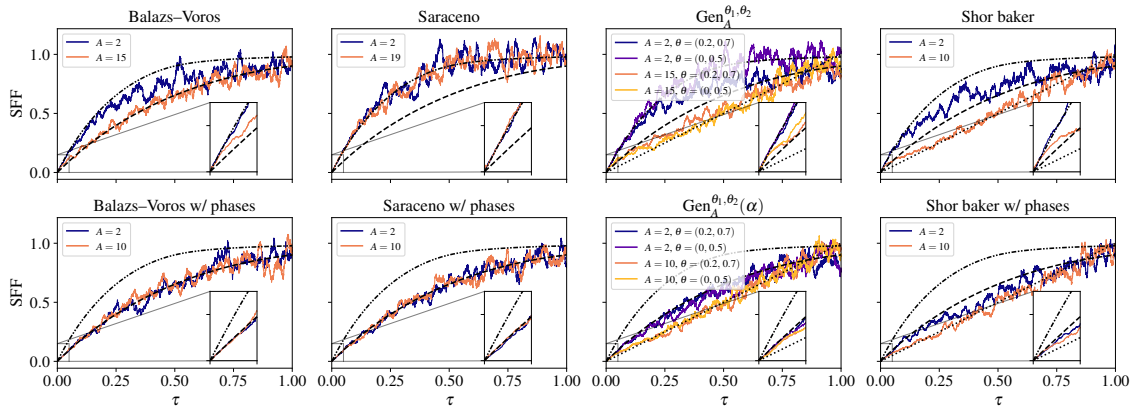


Figure 4: Averaged SFFs for the different quantizations of the  $A$ -baker's maps, for  $N = 9690$ . In the top row of standard phaseless quantizations, the very early time SFF follows the 2-block COE behavior (slope 4 at the origin), while for the bottom row of phase variant quantizations, the early time SFF has slope 2. All insets show up to  $\tau = 0.05$ , or up to  $t = 484$  for  $N = 9690$ . For several of the larger  $A$  quantizations, the transition away from the early time ( $\tau \approx 0$ ) SFF slope behavior is already visible in this window. In general, the larger time SFF, corresponding to shorter range spectral statistics like the level spacings, vary greatly depending on the particular quantization.

312 and CUE, we just take  $F(t)$  to be the same as  $f(t)$  in Eq. (9). We plot the resulting level spacing  
 313 statistics and SFF of the intermediate matrices  $F(t)$  for different values of  $t$  in Fig. 6, which  
 314 show similar behavior as the statistics shown in Fig. 3 and 4.

### 315 3.3 Periodic orbit expansion

316 We now briefly analytically explain the above numerical observations for the early time SFF  
 317 slope using a semiclassical periodic orbit expansion for the SFF of the  $A$ -baker's map quantiza-  
 318 tions [59, 62, 63], leaving the full details for Sec. 6. This analysis fills in the SFF slope values  
 319 for the entirety of Tab. 2, and moreover identifies the precise measure zero set of phases  $\alpha$  that  
 320 lead to an SFF slope of 4 rather than 2. The slope 2 results we obtain for the specific models  
 321 here differ from the usual periodic orbit theory expectation for generic systems, where one  
 322 expects the early time SFF slope to faithfully reflect the number of symmetry sectors of the  
 323 classical system [10, 47]. For the Saraceno quantization, which ends up as part of the mea-  
 324 sure zero set leading to the slope of 4, the SFF slope of 4 was derived in [62]. In the models  
 325 here, the addition of phases alters the semiclassical trace formula as seen below, which can  
 326 produce the SFF slope of 2. For the Shor baker quantizations, complications also arise due to  
 327 the different generalized DFT blocks. This requires a more complicated analysis of the  $t$ -step  
 328 propagator (Sec. 6.3, Appendix D), which we determine using coherent state evolution, in  
 329 order to derive the corresponding trace formula.

330 In all of the following,  $t \in \mathbb{N}$ , and  $N$  will be a multiple of  $A^t$  for convenience. As we are  
 331 interested in the SFF slope for early times  $\tau = t/N$  as  $N \rightarrow \infty$ , we will assume  $t \rightarrow \infty$  slowly,  
 332 such as at a rate  $\sim \log_A N$  or slower (so that  $N$  can still be a multiple of  $A^t$ ); this corresponds  
 333 to  $\tau \rightarrow 0$ . We start with a matrix  $\hat{U}_N = \hat{U}_N(\alpha)$  from the Generic phase variant quantization

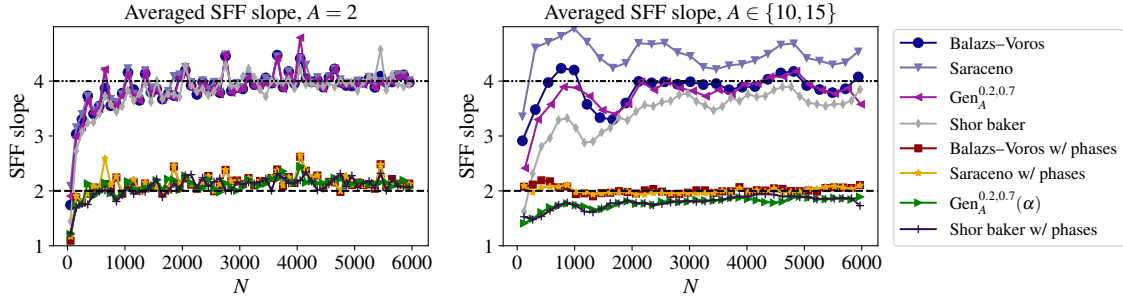


Figure 5: Averaged best fit early time SFF slope for  $A = 2$  (left) and  $A \in \{10, 15\}$  (right,  $A = 15$  for standard Balazs–Voros, Saraceno, and  $\text{Gen}_{A=15}^{0.2,0.7}$  quantizations, and  $A = 10$  for the remaining). The quantizations with random phases show a slope near 2, while those without show a slope near 4. Some of the quantizations shown share the random choice of phases. Outliers where the least squares fitting had large error were removed prior to averaging (cf. Fig. 10, Appendix C).

334  $\text{Gen}_A^{\theta_1, \theta_2}(\alpha)$  (which includes the Balazs–Voros and Saraceno phase quantizations),

$$\hat{U}_N = (\hat{F}_N^{\theta_1, \theta_2})^{-1} \bigoplus_{j=0}^{A-1} e^{2\pi i \alpha_j} \hat{F}_{N/A}^{\theta_1, \theta_2}. \quad (10)$$

335 One can readily check that applying the semiclassical propagator and saddle point method  
 336 described in [63] (see also [62] and Eq. (D.2)) with these phases yields the periodic orbit  
 337 approximation for  $N \rightarrow \infty$ ,

$$\text{tr} \hat{U}_N^t \approx \sum_{\nu=0}^{A^t-1} \frac{1}{A^{t/2}} e^{2\pi i N S_\nu} e^{2\pi i \sum_{j=0}^{A-1} \alpha_j \eta_j(\nu)}, \quad (11)$$

338 where  $S_\nu := \frac{\nu \bar{\nu}}{A^t - 1}$  is the classical action,  $\bar{\nu}$  is the (length  $t$ ) base  $A$  reversal of  $\nu$ , and  $\eta_j(\nu)$  is  
 339 the number of  $j$ 's in the (length  $t$ ) base  $A$  expansion of  $\nu$ . To estimate the SFF  $\frac{1}{N} |\text{tr} \hat{U}_N^t|^2$ , one  
 340 expands Eq. (11) in a double sum over indices  $\nu, \sigma$ , and takes the “diagonal approximation” [9]  
 341 with symmetry factors: The two classical symmetries are time-reversal  $\nu \mapsto \bar{\nu}$  and reflection  
 342  $R(\nu) = A^t - 1 - \nu$ . Only summing over the orbits  $\sigma \in \{\nu, \bar{\nu}, R(\nu), R(\bar{\nu})\}$  and their cyclic rotations  
 343 results in

$$\frac{1}{N} |\text{tr} \hat{U}_N^t|^2 \approx \frac{2t}{N} + \frac{2t}{NA^t} \left( \sum_{j=0}^{A-1} e^{2\pi i (\alpha_j - \alpha_{A-1-j})} \right)^t. \quad (12)$$

344 We find that in order for the second term of Eq. (12) not to decay as we average over  $t \rightarrow \infty$ ,  
 345 we must have  $\alpha_j = \alpha_{A-1-j}$  (modulo 1) for all  $j$ . Thus we obtain an SFF slope of 4 in this case,  
 346 and a slope of 2 in all other cases. The requirement  $\alpha_j = \alpha_{A-1-j}$  preserves a kind of “block”  
 347  $R$ -symmetry, even though in general such quantizations can break the microscopic  $R$ -symmetry  
 348  $|x\rangle \mapsto |N-1-x\rangle$ .

349 The standard phaseless quantizations here have  $\alpha_j = 0$  for all  $j$ , and thus meet the require-  
 350 ment for an SFF slope of 4, in agreement with numerics. We also note that when  $\alpha_j = \alpha_{A-1-j} + 1/2$   
 351 (mod 1), the approximation in Eq. (12) gives the value *zero* for the SFF at odd times  $t$ . In fact,  
 352 this is exact for the Saraceno phase variant with these phases: When  $\alpha_j = \alpha_{A-1-j} + 1/2$ , then  
 353 the resulting Saraceno  $\hat{U}_N(\alpha)$  *anticommutes* with the reflection operator  $R_N : |x\rangle \mapsto |N-1-x\rangle$ ,  
 354 so that every eigenvalue  $e^{i\lambda}$  comes with a partner  $-e^{i\lambda}$ , and  $\text{tr} \hat{U}_N^t = 0$  for odd  $t \in \mathbb{N}$ .

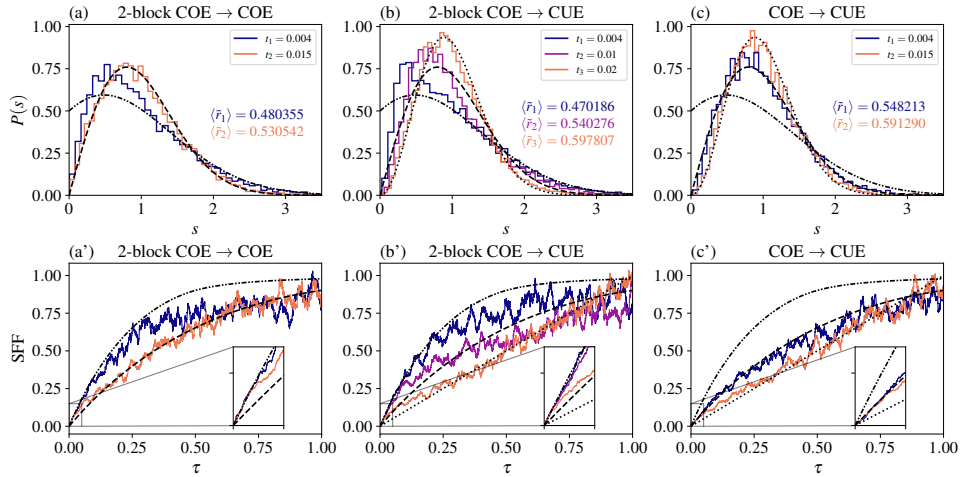


Figure 6: Level spacing histograms (top row) and SFFs (bottom row) for random instances of the Rosenzweig–Porter-like interpolation  $F(t)$  (defined in the paragraph below Eq. (9)), for  $N = 9690$ . Each column involves two or three independent random matrices  $F(t)$ , one chosen for each  $t$  value. Different values of  $t$  appear to describe the various level spacings and SFF behaviors seen in Figs. 3 and 4.

355 We now consider the Shor baker phase variant quantizations. Unlike the  $\text{Gen}_A^{\theta_1, \theta_2}(\alpha)$  phase  
 356 variant quantizations, we recall this quantization involves different generalized DFT matrices  
 357 for each block,

$$\hat{U}_N = \hat{F}_N^{-1} \left( \bigoplus_{j=0}^{A-1} e^{2\pi i \alpha_j} \hat{F}_{N/A}^{0, -j/A} \right). \quad (13)$$

358 In order to estimate the SFF using the periodic orbit expansion, we must first identify  
 359 the correct  $t$ -step quantization  $\hat{U}_N^{(t)}$  corresponding to this  $\hat{U}_N$ , which is complicated by the  
 360 different generalized DFT blocks. By determining the behavior of  $\hat{U}_N(\alpha)$  on maximally lo-  
 361 calized coherent states (Sec. 6.3), we can find the corresponding  $t$ -step propagator in mixed  
 362 momentum-position basis (Eq. (39)), which is used to derive the trace formula (Eq. (41)),

$$\text{tr} \hat{U}^{(t)} \approx \sum_{\nu=0}^{A^t-1} \frac{1}{A^{t/2}} e^{2\pi i N S_\nu} e^{\frac{2\pi i \nu \bar{\nu}}{A^t(A^t-1)}} e^{-2\pi i \frac{\phi(\nu)}{A}} e^{2\pi i \sum_{j=0}^{A-1} \alpha_j \eta_j(\nu)},$$

363 where  $\phi(\nu) = -\sum_{j=2}^t \alpha_j \sum_{i=1}^{j-1} \alpha_i A^{-j+i}$ . As calculated in Sec. 6.3, the extra factors in the trace  
 364 formula, with the diagonal approximation, eventually yield

$$\frac{1}{N} |\text{tr} \hat{U}_N^t|^2 \approx \frac{2t}{N} + \frac{2t}{NA^t} \left( \sum_{j=0}^{A-1} e^{2\pi i (\alpha_j - \alpha_{A-1-j} + 2j/A)} \right)^t e^{2\pi i t/A}. \quad (14)$$

365 Similar analysis then shows we obtain an averaged SFF slope of 4 iff

$$\alpha_{A-1-j} = \alpha_j + \frac{2j+1}{A} \pmod{1}, \quad j \in \llbracket 0 : A-1 \rrbracket, \quad (15)$$

366 and slope 2 in all other cases. For the standard Shor baker quantization,  $\alpha_j = j^2/A$ , which  
 367 satisfies Eq. (15). Unlike the condition on phases for the Balazs–Voros, Saraceno, and generic  
 368 quasiperiodic quantizations, this condition does not seem to exhibit a clear “block”  $R$ -symmetry  
 369 to mirror the classical one.

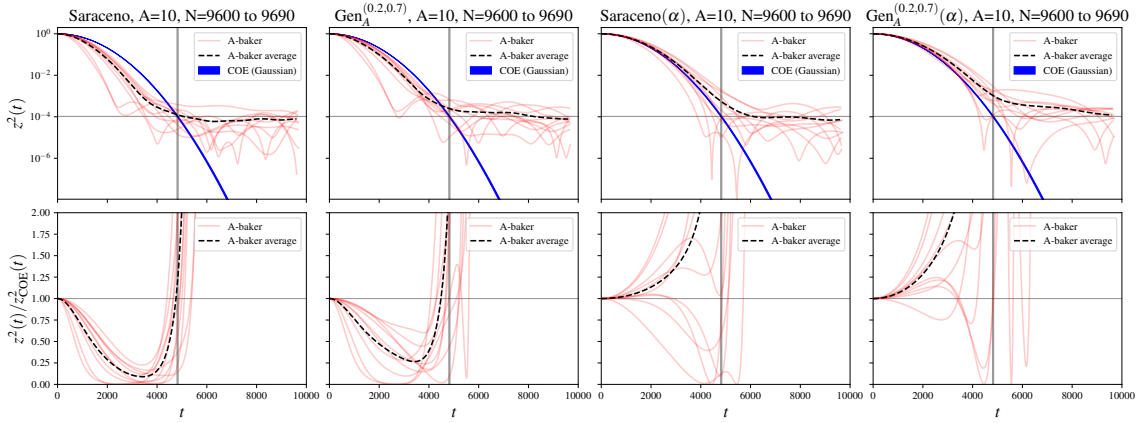


Figure 7: Effect of spectral anomalies on quantum cyclic ergodicity measured in terms of the persistence  $z^2(t)$ , via four different quantizations of  $A = 10$ -baker's maps with different kinds of anomalies. The depicted quantizations are Saraceno (no anomalies),  $\text{Gen}_A^{(0.2,0.7)}$  (weak reflection and time-reversal anomalies),  $\text{Saraceno}(\alpha)$  (strong reflection anomaly) and  $\text{Gen}_A^{(0.2,0.7)}(\alpha)$  (strong reflection anomaly, weak time-reversal anomaly). All values of  $N$  from 9600 to 9690, in steps of 10, are depicted (translucent red lines) together with the average  $z^2(t)$  (top row) and  $z^2(t)/z_{\text{COE}}^2(t)$  (bottom row) over these values of  $N$  (dashed black line) to observe the statistical trends after averaging out the strong fluctuations with  $N$ . *Top row*: The persistence  $z^2(t)$  given by Eq. (19) is plotted as a function of time  $t$  in a log-linear scale, and compared with the COE (Gaussian) curves  $z_{\text{COE}}^2(t)$  denoting the ideal behavior of COE statistics given by Eq. (21) over these values of  $N$  [up to  $O(N^{-1})$  fluctuations, which are not depicted for the COE reference]. The vertical band near the center of each plot depicts the range of  $t = N/2$  over the different values of  $N$ , and the horizontal band depicts  $z^2(t) = N^{-1}$  (representing the order of magnitude of  $\eta^2(N) = cN^{-1}$ ), the value reached by the COE (Gaussian) curve at  $t = N/2$  (the cutoff time for cyclic ergodicity). *Bottom row*: The ratio  $z^2(t)/z_{\text{COE}}^2(t)$  is plotted against  $t$  in a linear-linear scale, with the vertical band near the center again depicting the range of  $t = N/2$ , while the horizontal line near the center depicts a unit ratio, i.e.,  $z^2(t) = z_{\text{COE}}^2(t)$ . The rapid increase near  $t = N/2$  in these plots represents the onset of  $O(N^{-1})$  fluctuations as the dominant behavior of  $z^2(t)$  around and beyond this time. These plots appear consistent with quantum cyclic ergodicity of the kind associated with COE [ $z^2(t) \geq z_{\text{COE}}^2(t)$  up to  $O(N^{-1})$  fluctuations], resulting from strong anomalies (symmetry breaking in long-range measures) but not weak anomalies as explained in the text.

### 370 3.4 Symmetry breaking and quantum dynamical ergodicity

371 Having demonstrated that measures of spectral statistics can be incompatible with classical  
 372 symmetries, we now consider the direct relation between spectral statistics and quantum dy-  
 373 namics in the Hilbert space. This is especially of interest in illustrating the fully quantum  
 374 mechanical role of spectral anomalies or deviations from ideal random matrix behavior, irre-  
 375 spective of symmetries in the classical limit. We will take advantage of the distinct behavior  
 376 of each measure across different quantizations of the  $A$ -baker's maps to contrast the role of  
 377 short-range and long-range spectral statistics in influencing quantum dynamics. In particular,  
 378 we will provide numerical evidence that long-range symmetry breaking or strong anomalies  
 379 are sufficient to induce ergodicity (in a sense to be clarified below) in the quantum dynam-  
 380 ics of the system, while short-range or weak anomalies have a milder effect that may not be



381 significant in the  $N \rightarrow \infty$  limit.

382 For this purpose, we will consider the notion of quantum cyclic ergodicity in the Hilbert  
 383 space, introduced in Ref. [27] as a direct quantum dynamical counterpart to spectral statistics.  
 384 There, it was shown that the presence of sufficient long-range spectral rigidity is tied to the  
 385 existence of an orthonormal basis  $\{|C_k\rangle\}_{k=0}^{N-1}$  where every initial state “visits” every other state  
 386 in a cyclic sequence. This form of ergodicity is appropriate for time-independent unitary sys-  
 387 tems with (quasi-)energy conservation, and differs from more direct forms related to classical  
 388 ergodicity possible in open or time-dependent quantum systems [64–66]. Quantitatively, the  
 389 overlap of an initial state  $|C_k\rangle$  with  $|C_{k+t}\rangle$  after  $t$  time-steps, called the persistence,

$$z_k^2(t) \equiv |\langle C_{k+t} | \hat{U}_N^t | C_k \rangle|^2, \quad (16)$$

390 must be larger than a cutoff  $\eta^2(N) = cN^{-1}$  (where  $c$  is some  $\Omega(1)$  parameter) associated with  
 391 the overlap of random states for  $t \in [-N/2, N/2]$ , i.e.,

$$z_k^2(t) > \eta^2(N), \forall t \in \left[-\frac{N}{2}, \frac{N}{2}\right]. \quad (17)$$

392 Further, the “optimal” orthonormal basis in which this property is most likely to be present [in  
 393 terms of maximizing  $z_k^2(1)$ ] was shown to be given by the discrete Fourier transform (DFT) of  
 394 the energy eigenstates:

$$|C_k\rangle = \frac{1}{\sqrt{N}} \sum_{n=0}^{N-1} e^{-2\pi i kn/N} |E_n\rangle, \quad (18)$$

395 where the energies are sorted in ascending order. In this case,  $z_k^2(t) = z^2(t)$  for all  $k$ , given in  
 396 terms of the energy levels by

$$z^2(t) = \left| \frac{1}{N} \sum_{n=0}^{N-1} e^{i(E_n - 2\pi n/N)t} \right|^2. \quad (19)$$

397 This is the basis we will study numerically.

398 For “ideal” RMT-like behavior,  $z_{\text{RMT}}^2(t) = \exp[-\Delta^2 t^2]$  to leading order [27] (originating in  
 399 Gaussian spectral fluctuations [67–69]), where (specializing to even  $N$  for simplicity)

$$\Delta^2 = 2 \sum_{t=1}^{N/2} \frac{\text{SFF}(t)}{N t^2} \quad (20)$$

400 gives the leading contribution to spectral fluctuations in various measures of long-range spec-  
 401 tral rigidity such as the Dyson-Mehta  $\Delta_3$  parameter [3] or the related  $\Delta^*$  [70] that measure  
 402 the regularity of the spectrum. For COE, one obtains

$$z_{\text{COE}}^2(t) = e^{-4t^2 \ln N / N^2}. \quad (21)$$

403 This is guaranteed to exceed  $\eta^2(N) = cN^{-1}$  as per Eq. (17) with the slight restriction  $|t| < N(1-\epsilon)/2$   
 404 (for any small  $\epsilon > 0$ ), showing that each  $|C_k\rangle$  in a system with ideal COE statistics “ergodically”  
 405 visits almost all basis vectors  $|C_{k-N/2}\rangle$  through  $|C_{k+N/2}\rangle$  in succession. Due to the presence of  
 406 time-reversal symmetry without separate sectors in COE [1], one cannot here demand ergod-  
 407 icity in the full interval  $|t| \leq N/2$  in Eq. (17), corresponding to fully visiting every single basis  
 408 vector, that is present [27] in CUE or a non-degenerate half of CSE.

409 In Fig. 7, the persistence  $z^2(t)$  in the DFT basis for 4 different quantizations of the  $A = 10$ -  
 410 baker map [Saraceno and Gen $_A^{(0.2,0.7)}$ , with and without phases] are compared to the ideal COE  
 411 persistence, to examine their quantum dynamical ergodicity relative to the behavior of COE

[i.e., if  $z^2(t) \geq z_{\text{COE}}^2(t) + O(N^{-1})$ ]. We recall that while the unitary reflection symmetry may be broken weakly or strongly in these quantizations, the antiunitary time reversal symmetry is always broken only weakly in the spectral statistics, making COE the appropriate standard for comparison. The choice of  $A = 10$  statistically guarantees that the Berry-like phases  $\alpha_j$  are generically random, as required for strong anomalies (for instance, in Eq. (14)); in contrast,  $A = 2$  has only one independent phase and may show a significant dependence on this phase as seen in Fig. 10(g). Further, due to atypical fluctuations with varying  $N$  in the level statistics of baker maps [see, e.g., Fig. 8 and Fig. 10(a)-(f)], noted as far back as Ref. [49], we consider statistical trends over 10 adjacent values of  $N$ , and additionally plot the persistence  $z^2(t)$  averaged over these values of  $N$  to tame the fluctuations. This is justified for our numerics as  $N$  varies only by around 1% in our chosen range. Subsequently, we observe if the average persistence is comparable to (or is greater than) the ideal COE trend to diagnose ergodicity in the presence of a long-range time-reversal symmetry.

The numerical trends are as follows:

1. For Saraceno (no anomalies) and  $\text{Gen}_A^{(0.2,0.7)}$  (weak reflection and time-reversal anomalies),  $z^2(t)$  remains less than  $z_{\text{COE}}^2(t)$  up to random fluctuations consistent with  $O(N^{-1})$ , showing compatibility with ergodicity-breaking in the presence of a long-range reflection symmetry.
2. For Saraceno with phases (strong reflection anomaly) and  $\text{Gen}_A^{(0.2,0.7)}$  with phases (strong reflection anomaly and weak time-reversal anomaly),  $z^2(t)$  fluctuates around  $z_{\text{COE}}^2(t)$ , showing compatibility with the presence of COE-type ergodicity without a long-range reflection symmetry (but with time-reversal indicated by long-range spectral statistics).

Finally, we note that in both the  $\text{Gen}_A^{(0.2,0.7)}$  cases (with or without phases), which possess a weak time-reversal anomaly,  $z^2(t)$  oscillates around a slightly larger value than in the Saraceno cases (which have an unbroken time-reversal symmetry), though this slight increase does not statistically appear to be sufficient to induce ergodicity without strong anomalies. In fact, this slightly larger value is likely a finite size numerical effect for these values of  $N$ , stemming from the logarithmic divergence of  $\Delta^2$  with  $N$  in Eq. (20) for a linear ramp  $\text{SFF}(t) \propto t$  leading to a visible numerical contribution from the late-time regime (corresponding to the crossover in Sec. 3.2). However, one can show that in the  $N \rightarrow \infty$  limit, as long as the SFF appreciably deviates from the early-time trend (due to weak anomalies) only for  $|t| \geq cN$  in  $\text{SFF}(t)$ , the anomalous contribution to  $\Delta^2$  is subleading compared to the early-time contribution; it is indeed for a similar reason that COE possesses logarithmically divergent ( $\ln N$ ) spectral fluctuations [3, 9, 70] despite the SFF deviating from a linear ramp [1] for  $t \sim N$ . To see this quantitatively, we consider a simplified model with the interval of summation  $t \in \mathcal{I} = [1, N/2]$  split into an early-time regime  $\mathcal{I}_{\text{UV}} = [1, cN]$  with  $\text{SFF}(t) = \alpha t$ , and a late-time regime  $\mathcal{I}_{\text{IR}} = (cN, N/2]$  with  $\text{SFF}(t) = \beta t$  for some  $c \ll 1$ ; in this case, the leading contribution to the logarithmic divergence  $\alpha \ln(cN/1)$  comes entirely from the early time region, while the late-time region contributes a subleading term proportional to  $\beta \ln[(N/2)/(cN)] = -\beta \ln(2c)$ . Nevertheless, other effects (such as a deviation from a Gaussian profile of  $z^2(t)$ ) are possible at larger  $N$ , and it would be interesting to explore or rule out such phenomena at values of  $N$  at least an order of magnitude larger than the present study.

In summary, our numerics for  $N \approx 10^4$  in quantizations of  $A$ -baker's maps with different manifestations of spectral anomalies appear to be consistent with a direct link between long-range symmetry breaking (strong anomalies) and cyclic ergodicity, with an at best weaker effect of short-range symmetry-breaking (weak anomalies), verifying the analytical connection obtained in Ref. [27] between long-range spectral statistics and quantum dynamical ergodicity.

## 4 Operator symmetries and level spacing statistics

In the remaining sections, we provide further background and details for the results in the previous section. We start with the relation between the quantizations' operator symmetries and the classical map's symmetries.

### 4.1 Operator symmetries

Classifying quantum symmetries corresponding to the classical symmetries in these models is not entirely straightforward. If one can construct a quantum version of the classical symmetry, such as in the Saraceno quantization [50], then one can say that the quantization preserves the corresponding classical symmetry. However, due to the infinite possibilities of quantum operators that can all correspond to same the classical symmetry operator in the limit  $\hbar \rightarrow 0$  ( $N \rightarrow \infty$ ), verifying that a quantization does not commute with any of those operators is much less clear. For this reason, we will discuss a limited version of the possible operator symmetries, and include more detailed analysis in Appendix A. These restricted definitions will still agree with those historically used to describe the symmetries of the Balazs–Voros and Saraceno quantizations [49, 50].

*Quantization on the torus*— To discuss the relation between the classical symmetries and operator symmetries, we first provide more background on the quantization process on the torus. For further details, see [60, 71]. Quantization on the 2-torus associates to each natural number  $N \in \mathbb{N}$  and  $\theta \in [0, 1]^2$  an  $N$ -dimensional Hilbert space  $\mathcal{H}_N(\theta)$  of quantum states. The parameter  $\theta = (\theta_1, \theta_2)$  sets the quasiperiodicity requirement in position and momentum as follows. Letting  $S(q, p) = e^{i(pQ - qP)/\hbar}$  denote the phase space translation operators, then the Hilbert space  $\mathcal{H}_N(\theta)$  is associated with states  $\psi$  on  $\mathbb{R}$  satisfying

$$S(1, 0)\psi = e^{-2\pi i\theta_1}\psi, \quad S(0, 1)\psi = e^{2\pi i\theta_2}\psi,$$

for  $\theta = (\theta_1, \theta_2)$ . Recall the Balazs–Voros quantization corresponds to the case  $\theta_1 = \theta_2 = 0$  which describes periodic states, while the Saraceno quantization corresponds to  $\theta_1 = \theta_2 = 1/2$  which describes antiperiodic states. The generic quantization  $\text{Gen}_A^{\theta_1, \theta_2}$  corresponds to the quasiperiodic conditions described by  $\theta = (\theta_1, \theta_2)$ . The main consideration we need for different  $\theta$  is that position representation states  $|n\rangle$  and momentum representation states  $|k\rangle$  are related via the generalized discrete Fourier transform  $\hat{F}_N^{\theta_1, \theta_2}$  as defined in Eq. (5), which depends on  $\theta$ . This explains why one uses the generalized DFT matrices in the Saraceno and  $\text{Gen}_A^{\theta_1, \theta_2}$  quantizations. The generalized DFT matrix relation between position and momentum also implies that operators on  $\mathcal{H}_N(\theta)$ , which are  $N \times N$  matrices, are converted between position and momentum basis via conjugation by  $\hat{F}_N^{\theta_1, \theta_2}$  (or its inverse).

The Shor baker quantizations involve several different generalized DFT blocks, but we will associate these quantizations with periodic boundary conditions to match the  $\hat{F}_N^{-1}$  factor.

*Reflection symmetry*— Let  $B$  be the classical A-baker's map, and recall the classical reflection symmetry  $R$  in Eq. (2), which maps  $(q, p)$  to  $(1 - q, 1 - p)$  and satisfies  $RBR^{-1} = B$ . Its quantum analogue  $R_N$  should then reverse, in some way, both the position states  $|n\rangle$  and the momentum states  $|k\rangle$ , and quantizations  $\hat{U}_N$  that preserve the reflection symmetry should satisfy  $R_N \hat{U}_N R_N^{-1} = \hat{U}_N$ .

For the Saraceno quantizations, which we will denote here by  $\hat{B}_{N,A}^{\text{Sar}}$ , the quantum reflection is  $R_N : |x\rangle \mapsto |N - 1 - x\rangle$ , which has the same action in momentum space and commutes with  $\hat{B}_{N,A}^{\text{Sar}}$  since  $R_N = (\hat{F}_N^{\frac{1}{2}, \frac{1}{2}})^2$ . One can separate the eigenvalues of  $\hat{B}_{N,A}^{\text{Sar}}$  according to whether its corresponding eigenstate is in the  $+1$  or  $-1$  symmetry sector of  $R_N$ , and this produces COE level spacing statistics within each symmetry sector, as explained in [50]. (See Fig. 9 for larger A.) Additionally, when considering the spectrum as a whole, the two symmetry sectors

504 of the Saraceno quantizations combine to look like that of a direct sum of two COE matrices,  
 505 indicating that the two symmetry sectors behave essentially as if they are independent of each  
 506 other.

507 On the other hand, the Balazs–Voros, generic quasiperiodic, and Shor baker quantiza-  
 508 tions do not exhibit a clear analogous reflection symmetry. We investigate possible *Fourier*  
 509 reflection symmetries in Appendix A, and provide numerical plots demonstrating the lack  
 510 of Fourier reflection symmetry for the non-Saraceno quantizations that we consider (Balazs–  
 511 Voros,  $\text{Gen}_A^{0,2,0.7}$ ,  $\text{Gen}_A^{0,0.5}$ , and Shor baker). While this rules out a class of reflection operators  
 512 coming from the generalized DFT matrices, it does not prohibit the possibility of a different  
 513 commuting reflection-like operator in the  $N \rightarrow \infty$  limit. In Appendix A, we also briefly con-  
 514 sider the symmetries of phase space (Husimi) plots of the eigenvectors.

515 *TR symmetry*—The other classical symmetry is a time reversal (TR) symmetry  $T : (q, p) \mapsto (p, q)$ ,  
 516 which satisfies  $TBT^{-1} = B^{-1}$ . Its quantum analogue should act on operators by switching  
 517 between position and momentum basis, and mapping  $i \mapsto -i$ , so that quantizations  $\hat{U}_N$  (in  
 518 position basis) preserving TR symmetry should ideally satisfy the antiunitary relation

$$\hat{F}_N^{\theta_1, \theta_2} \hat{U}_N (\hat{F}_N^{\theta_1, \theta_2})^{-1} = (\hat{U}_N^{-1})^*, \quad (22)$$

519 where  $*$  denotes entrywise complex conjugation. We can define a quantization  $\hat{U}_N$  to have  
 520 an “operator TR symmetry” if it satisfies Eq. (22) for its corresponding boundary conditions  
 521  $\theta$ . However, as for the reflection symmetry, other antiunitary operations with the same clas-  
 522 sical limit could also be a valid “quantum TR symmetry”. For the quantizations we consider,  
 523 the Balazs–Voros and Saraceno quantizations satisfy Eq. (22), while the generic quasiperiodic  
 524 quantizations with  $\theta_1 \neq \theta_2$  and the Shor baker quantizations do not.

## 525 4.2 Level spacing statistics

526 To investigate the level spacing statistics of an  $N \times N$  unitary matrix, one orders the eigenangles  
 527  $\theta_i$ , and defines the nearest neighbor level spacings (or gaps)

$$s_i = \theta_{i+1} - \theta_i, \quad i \in \mathbb{Z}/N\mathbb{Z}. \quad (23)$$

528 To compare the distribution of these level spacings to the expected universal RMT distributions,  
 529 the normalization is to multiply the  $(s_i)$  by  $\frac{N}{2\pi}$ , which we do for all level spacing histogram plots.

530 The mean (adjacent) gap ratio statistic, as defined in [44], is given by

$$\langle \tilde{r} \rangle = \left\langle \min \left( \frac{s_{i+1}}{s_i}, \frac{s_i}{s_{i+1}} \right) \right\rangle_i, \quad (24)$$

531 where the average is over all  $i \in \mathbb{Z}/N\mathbb{Z}$ . This statistic provides a single value that can be  
 532 used to compare the closeness to RMT level spacings, and does not require any normalization  
 533 or unfolding of the eigenvalues. The mean gap ratios for the standard RMT ensembles in  
 534 the  $N \rightarrow \infty$  limit were derived in [61], and for block RMT matrices in [48]. The block  
 535 RMT matrices are relevant in the presence of discrete symmetries, as one generally needs to  
 536 separate eigenstates according to the symmetry sector to recover expected non-block RMT  
 537 level statistics. We are primarily concerned with the circular orthogonal ensemble (COE) and  
 538 circular unitary ensemble (CUE). Since the circular ensembles and Gaussian ensembles have  
 539 the same local  $n$ -level correlation functions in the limit  $N \rightarrow \infty$  [3], we may interchange terms  
 540 such as “COE level spacings” and “GOE level spacings”. We list the values of relevance to our  
 541 study in Tab. 3.

542 Here the 2-block GOE matrix means a direct sum of two equal sized, independent GOE  
 543 matrices, and similarly for the the 2-block GUE matrix.

	GOE	2-block GOE	GUE	2-block GUE	Poisson
$\langle \tilde{r} \rangle$	0.53590	0.423415	0.60266	0.422085	0.38629

Table 3: Mean gap ratio values for RMT ensembles, from [48, 61].

In general, one expects that chaotic systems with time reversal (TR) symmetry have GOE/COE spectral statistics, while those without have GUE/CUE statistics. Additionally, one expects the presence of discrete symmetries to produce block-RMT statistics, according to the number of symmetry sectors. As we saw for the  $A$ -baker's map however, the actual level spacings behavior can be highly variable depending on the particular quantization.

We plot in Fig. 8 the mean gap ratios for the different quantizations over a range of  $N \in \mathbb{AN}$ . As we saw for specific dimensions  $N$  in Figs. 2 and 3, out of all the quantizations in Tab. 2, only the Saraceno quantizations, and the generic quantization  $\text{Gen}_{A=2}^{0,0.5}$  (for  $A = 2$  only), have mean gap ratio close to that for block COE matrices. We note that there are dips in the mean gap ratio at specific values of  $N$ , which typically correspond to powers of the slope  $A$ . For such dimensions the level spacings may look non-RMT (sometimes close to Poisson).

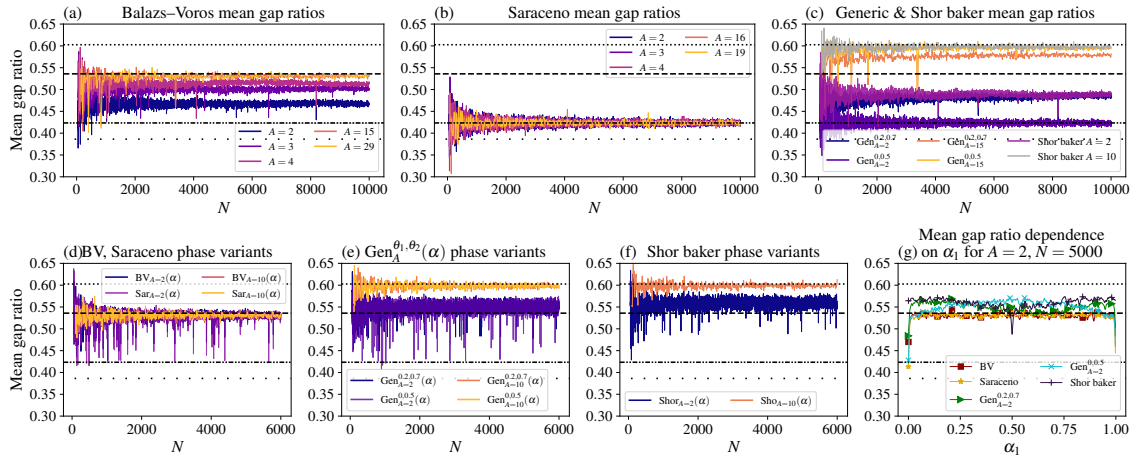


Figure 8: (a)–(f) Mean gap ratios for the different quantizations over  $N \in \mathbb{AN}$ . The horizontal lines (from top to bottom) are the RMT reference values for GUE (dotted), GOE (dash-dot-dotted), 2-block GOE (dashed), and Poisson (loosely dotted). Some of the phase variant quantizations may share the same random choice of phases. (g) Mean gap ratios for  $A = 2$  and  $N = 5000$  as a function of the phase  $\alpha = (0, \alpha_1)$  for  $\alpha_1 \in [0, 1)$  (step size 0.002). Note that  $\alpha_1 = 1/2$  corresponds to the standard Shor baker quantization, while  $\alpha_1 = 0$  corresponds to the standard versions of the other quantizations.

### 4.3 Approximate symmetry classes for the Balazs–Voros quantization

We now return to the Balazs–Voros-type quantizations of the  $A$ -baker's map, which we saw have level spacing statistics that can exhibit deviations from RMT and overlook the presence of classical symmetry sectors. We demonstrate how one can obtain roughly COE-like level spacings for the Balazs–Voros quantization in Eq. (3) ( $A = 2$ ) by separating the eigenvalues according to *approximate* symmetry classes of their eigenstates, which was suggested as a possible method in [49]. However, we will see in Sec. 5 using the SFF that this separation still retains significant irregularities.

Recall the reflection operator  $R_N : |x\rangle \mapsto |N - x - 1\rangle$  which commutes with the Saraceno

564 quantization and is equal to  $(\hat{F}_N^{\frac{1}{2}, \frac{1}{2}})^2$ . This is the permutation matrix with 1s on the top-right  
 565 to bottom-left diagonal, which has the trivial block decomposition

$$R_N = \begin{pmatrix} & & & R_{N/A} \\ & & & \\ & & R_{N/A} & \\ & & \dots & \\ R_{N/A} & & & \end{pmatrix}.$$

566 Since it commutes with the Saraceno quantization  $\hat{B}_{N,A}^{\text{Sar}}$ , this allowed for separating the eigen-  
 567 states of  $\hat{B}_{N,A}^{\text{Sar}}$  according to whether they fall in the +1 or −1 eigenspace of  $R_N$ , which recovers  
 568 RMT spectral statistics.

569 For the Balazs–Voros quantizations, this suggests considering a similar reflection-like op-  
 570 erator, the permutation

$$\tilde{R}_N = (\hat{F}_N^{0,0})^2 = \begin{pmatrix} 1 & 0 & \dots & 0 \\ 0 & \dots & 0 & 1 \\ \vdots & & 0 & 1 & 0 \\ \vdots & & 0 & 1 & 0 & 0 \\ & \dots & \dots & & \vdots \\ 0 & 1 & 0 & \dots & 0 \end{pmatrix}, \quad (25)$$

571 which is a natural reflection candidate (cf. Appendix A) when considering states that are  
 572 periodic in position and momentum (vs antiperiodic for Saraceno quantizations). The map  
 573  $\tilde{R}_N$  is equal to  $\hat{F}_N^2$  and sends  $|x\rangle \mapsto |-x\rangle$  (taken modulo  $N$ ). While  $\tilde{R}_N$  does not commute with  
 574  $\hat{B}_N$ , it is in some sense close to commuting with  $\hat{B}_N$ . In particular, we show in Appendix B that  
 575 the commutator  $[\hat{B}_{N,A}, \tilde{R}_N]$  has only very few non-decaying matrix elements.

576 Computing the overlap  $\langle \varphi^{(j)} | \tilde{R}_N | \varphi^{(j)} \rangle$  for all eigenvectors  $\varphi^{(j)}$  of  $\hat{B}_N$ , we create the two  
 577 symmetry classes,

$$S_+ = \{\varphi^{(j)} : \langle \varphi^{(j)} | \tilde{R}_N | \varphi^{(j)} \rangle \geq 0\},$$

$$S_- = \{\varphi^{(j)} : \langle \varphi^{(j)} | \tilde{R}_N | \varphi^{(j)} \rangle < 0\}. \quad (26)$$

578 We can then investigate the level spacing statistics within each approximate symmetry class,  
 579 which are shown (along with those for the exact Saraceno symmetry classes) in Fig. 9.

580 *Approximate symmetries for  $A = 2$* —As seen in Fig. 9(c)–(d), for  $A = 2$ , within a single  
 581 approximate symmetry class  $S_{\pm}$ , the level spacing statistics for the Balazs–Voros quantization  
 582 look approximately COE. The inner products  $\langle \varphi^{(j)} | \tilde{R}_N | \varphi^{(j)} \rangle$  tend to cluster near −1 and 1  
 583 (Fig. 9(e)), suggesting that while not exact,  $\tilde{R}_N$  is a fairly good choice of approximate symme-  
 584 try. Fig. 9(f) plots the quantity,

$$\frac{1}{N} \sum_{j=1}^N \left| \langle \varphi^{(j)} | \tilde{R}_N | \varphi^{(j)} \rangle - 1 \right|^2, \quad (27)$$

585 which is the mean square error of the inner product from  $\pm 1$ , for eigenstates of  $\hat{B}_N$ . Other than  
 586 some outliers that appear somewhat connected to powers of  $A$ , this error is fairly constant,  
 587 suggesting that the distribution shape shown for  $A = 2$  in Fig. 9(e) is likely representative for  
 588 other  $N$  as well.

589 We also note that attempting to use the Saraceno reflection operator  $R_N : |x\rangle \mapsto |N-x-1\rangle$   
 590 here for the Balazs–Voros quantization does not appear to produce any meaningful separation,  
 591 and the inner products  $\langle \varphi^{(j)} | R_N | \varphi^{(j)} \rangle$  are spread within  $[-1, 1]$  instead of clustering near  $\pm 1$ .



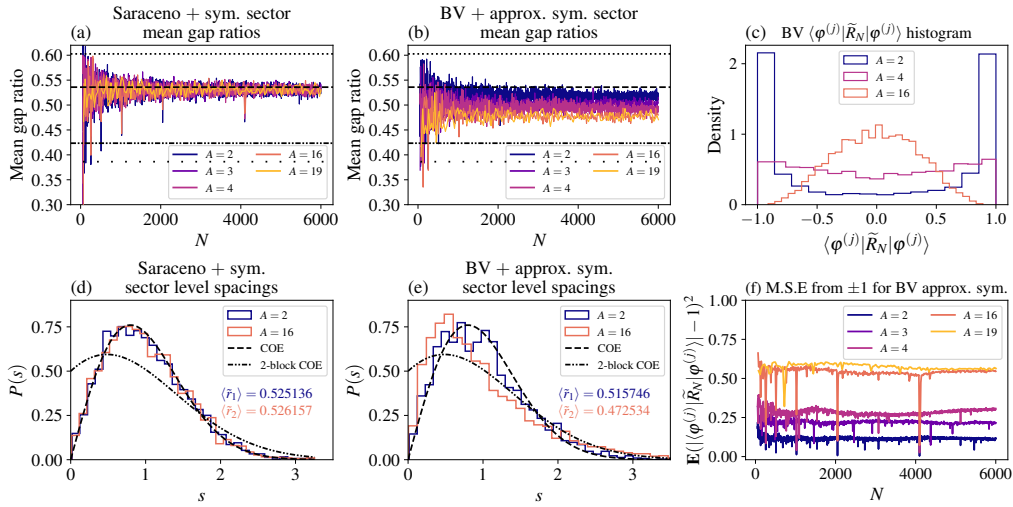


Figure 9: (a), (b) Mean gap ratios for the Saraceno + symmetry sectors and Balazs–Voros + approximate symmetry sectors, for  $N \in A\mathbb{N}$  even. (d), (e) Level spacing histograms for the Saraceno + symmetry sector and Balazs–Voros + approximate symmetry sector for  $N = 5904$ . (c) Balazs–Voros inner product histogram for  $N = 5904$  and  $A = 2, 4, 16$ . The histogram for  $A = 2$  shows a strong clustering split between  $+1$  and  $-1$ , but this dichotomy disappears for larger  $A$ . (f) The mean square error defined in Eq. (27) for the Balazs–Voros quantizations as a function of  $N$ .

592 *Failure for larger  $A$ -baker’s maps*— For  $A \geq 3$ , the Saraceno quantizations of the the  $A$ -  
 593 baker’s map continue to commute with the reflection operator  $R_N$ , and continue to exhibit  
 594 level spacing statistics that look like a direct sum of two COE matrices. Thus one can try to use  
 595 an approximate symmetry for the non-symmetrized Balazs–Voros quantizations with  $A \geq 3$   
 596 as well. Unlike the  $A = 2$  case however, the natural approximate symmetry candidate  $\tilde{R}_N$   
 597 does not produce even an approximately useful separation of eigenstates, as seen in Fig. 9(e).  
 598 The values  $\langle \varphi^{(j)} | \tilde{R}_N | \varphi^{(j)} \rangle$  no longer cluster strongly near  $\pm 1$ , and separating by the sign of  
 599  $\langle \varphi^{(j)} | \tilde{R}_N | \varphi^{(j)} \rangle$  does not reproduce RMT-like level statistics (Fig. 9(c)–(d)). Given that the  
 600 unseparated eigenvalue statistics begin to look more and more like a single COE matrix as  $A$   
 601 increases, this is not that surprising.

## 602 5 Spectral form factor analysis

603 In this section, we provide more detailed analysis and plots of the spectral form factor (SFF)  
 604 and its early time slope. Recall the SFF for an  $N \times N$  unitary matrix is given by the formula

$$\text{SFF}(t) = \frac{1}{N} |\text{Tr}(U_N^t)|^2 = \frac{1}{N} \sum_{j,k=1}^N e^{it(\theta_j - \theta_k)}, \quad (28)$$

605 and that we set  $\tau = t/N$ . The formula for the ensemble-averaged COE form factor [1] is

$$\langle \text{SFF}_{\text{COE}}(\tau) \rangle \equiv \lim_{N \rightarrow \infty} \frac{1}{N} \mathbb{E} |\text{Tr}(U_N^t)|^2 = \begin{cases} 2\tau - \tau \log(1 + 2\tau), & \tau \leq 1 \\ 2 - \tau \log\left(\frac{2\tau+1}{2\tau-1}\right), & \tau > 1 \end{cases}. \quad (29)$$

606 For the quantized baker’s maps, with no ensemble to average over, we average Eq. (28) at time  
 607  $t$  with its nearest  $2\ell$  neighbors (or from time 1 to  $2t - 1$  if  $t < \ell$ ), as described in more detail  
 608 in Appendix C.

609 We show plots of the early time SFF slope as function of the dimension  $N$  in Fig. 10(a)–  
 610 (f), corresponding to noisier, more detailed versions of the earlier Fig. 5. In general, the SFF  
 611 slope computations are noisy, and even the plots in Fig. 10 are averaged over the nearest  
 612  $\sim 20$  neighbors, after removing outliers which did not have a low error slope fit. These outliers  
 613 amount to only relatively few values of  $N$  for each quantization ( $< 1\%$  for  $A = 2$  quantizations,  
 614 and  $\sim 5\text{--}8\%$  for  $A = 10$  or  $15$  in Fig. 10). As in Fig. 5, we see in Fig. 10 a clear dichotomy in the  
 615 SFF slope between the standard phaseless quantizations and the phase variant quantizations.  
 616 In Fig. 10(g), we also plot the SFF slope for  $A = 2$  as a function of the phase parameter  
 617  $\alpha = (0, \alpha_1)$ , similarly as we did for the mean gap ratio in Fig. 8(g).

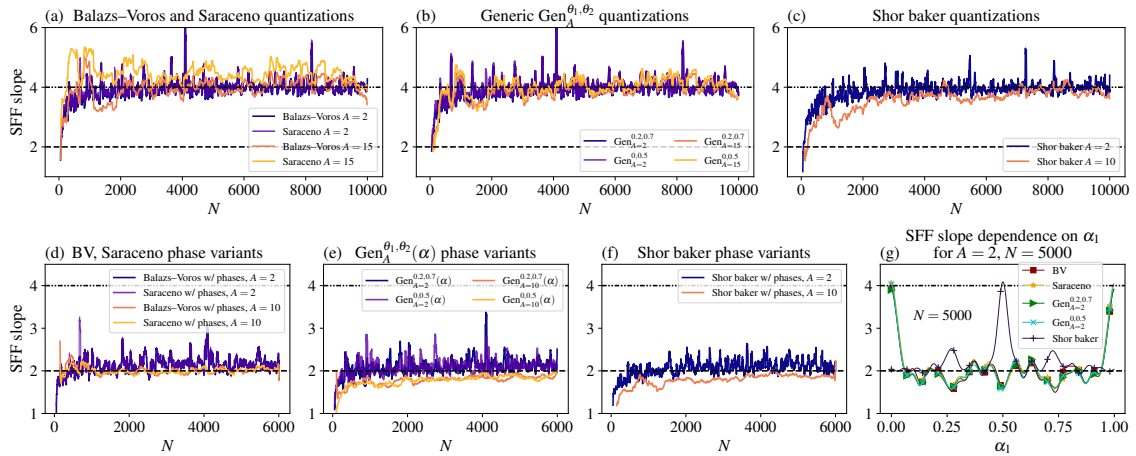


Figure 10: (a)–(c) Averaged early time SFF slope for the standard/phaseless quantizations, plotted as function of  $N \in \mathbb{N}$ . The SFF slope values cluster near 4. Outliers (fewer than 1% of points for  $A = 2$ , and  $\sim 5\text{--}8\%$  for  $A \in \{10, 15\}$ ) where the least squares slope fitting produced large residuals were removed before averaging. For further details, see Appendix C. (d)–(f) Averaged early time SFF slope for the phase variant quantizations, fewer than 1% of points removed as outliers. The SFF slope values cluster near 2. (g) SFF slope for  $A = 2$  and  $N = 5000$  as a function of the phase  $\alpha \in [0, 1)$  (step size 0.002) for the different types of quantizations. Compare with Fig. 8(g).

618 Next, in Fig. 11(a) we briefly examine the SFF within an individual approximate symmetry  
 619 class (Sec. 4.3) for the Balazs–Voros 2-baker quantization. We see that while the SFFs appear  
 620 to look COE for moderately sized  $\tau$ , there are irregularities near  $\tau = 0$ . Thus while separating  
 621 by the approximate symmetry class can partially restore level spacing statistics as in Fig. 9, it  
 622 produces long-range spectral irregularities. In contrast, for the Saraceno quantizations (not  
 623 shown), the SFF for an individual symmetry class appears to follow the single COE SFF for all  
 624  $\tau$ .

625 In Fig. 11(b) we also demonstrate a complication with determining the early time SFF  
 626 slope. For some values of  $N$ , the SFF may show large early time irregularities. Large enough  
 627 irregularities which do not have a good least squares fit are considered outliers, and we remove  
 628 such points prior to averaging and plotting in Figs. 5 and 10.

629 We note that some of the outliers and noise are products of the averaging methods used  
 630 to compute the SFF slope. While we do not optimize the averaging methods used, we choose  
 631 parameters so that it becomes clear whether the slope of the early time SFF is close to 2,  
 632 corresponding to the SFF for a single COE matrix, or close to 4, corresponding to the SFF for  
 633 a 2-block COE matrix. Due to this choice of parameters, along with the occasional outliers,  
 634 computing the SFF slope is not as convenient as computing the gap ratio statistic; however,

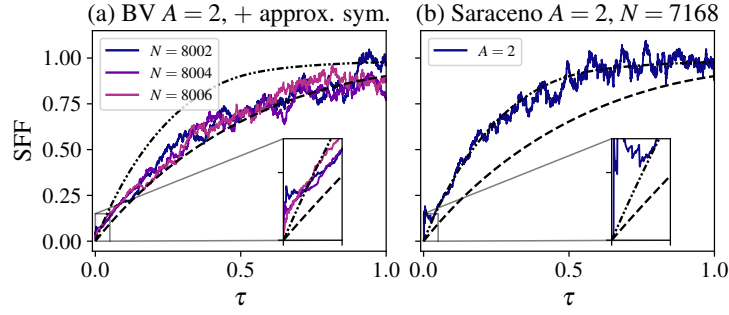


Figure 11: (a) Balazs–Voros SFF for + approximate symmetry classes for  $N = 8002, 8004$ , and  $8006$ . The behavior for small  $\tau$  shows irregularities, even though for larger times it follows the COE SFF. In contrast, the Saraceno  $\pm 1$  symmetry classes (not plotted) show single COE-like SFF. (b) Example of bad early time behavior in the SFF, for one of the rare outliers removed before averaging to produce the plots in Fig. 10.

635 for these models it proves to be more informative.

## 636 6 Semiclassical trace formula

637 In this section, we explain how one derives the semiclassical trace formulas used in Section 3.3.  
638 To that end, we must first revisit the classical  $A$ -baker’s map dynamics as used in [59, 62, 63].

### 639 6.1 Classical dynamics revisited

640 One particularly useful interpretation of the classical  $A$ -baker’s map is via its symbolic dy-  
641 namics [51]: Points  $(q, p) \in \mathbb{T}^2$  can be identified with infinite base  $A$  sequences of symbols  
642  $\dots a_{-2}a_{-1}a_0 \bullet a_1a_2\dots$ , where  $0.a_1a_2\dots$  is the  $A$ -ary expansion of  $q$ ,  $0.a_0a_{-1}a_{-2}\dots$  is the  $A$ -ary  
643 expansion of  $p$ , and  $\bullet$  is a separator distinguishing  $p$  from  $q$ . The classical  $A$ -baker’s map is  
644 then the 2-sided Bernoulli left shift,

$$\dots a_{-2}a_{-1}a_0 \bullet a_1a_2\dots \mapsto \dots a_{-1}a_0a_1 \bullet a_2a_3\dots$$

645 The composition of the  $A$ -baker’s map with itself  $t$  times is then given by  $t$  such shifts, or  
646 equivalently,

$$\begin{aligned} q &\mapsto A^t q - a_1 \cdots a_t, \\ p &\mapsto A^{-t}(p + a_t \cdots a_1), \end{aligned}$$

647 where digit expressions like  $a_1 \cdots a_t$  represent the value when viewed as a base  $A$  number,  
648  $a_1 \cdots a_t = \sum_{j=1}^t a_j A^{t-j}$ . The length  $t$  periodic orbits of the  $A$ -baker’s map are then seen to be  
649 given by  $A$ -ary expansions of the form  $\dots \nu \nu \cdot \nu \nu \cdots$  for any length  $t$   $A$ -ary string  $\nu = a_1 \cdots a_t$ .  
650 This corresponds to points,

$$q = \frac{\nu}{A^t - 1}, \quad p = \frac{\bar{\nu}}{A^t - 1},$$

651 where  $\bar{\nu} = a_t \cdots a_1$  denotes the  $A$ -ary reversal of  $\nu$ .

652 As determined in [62, 63], the classical action  $S_\nu$  of a point  $\nu$  is

$$S_\nu = \frac{\nu \bar{\nu}}{A^t - 1}. \quad (30)$$

653 Taken modulo 1, one has

$$S_\nu = S_{\bar{\nu}} = S_{R(\nu)} = S_{R(\bar{\nu})}, \quad (31)$$

654 where  $R(\nu)$  is the base  $A$  reflection operator  $R(\nu) = A^t - 1 - \nu$ . The reflection operator  $R$  acts  
655 on the expansion  $\nu = a_1 \cdots a_t$  by mapping each digit  $a_j$  to the digit  $A - 1 - a_j$ .

## 656 6.2 Periodic orbit theory for the Generic quantizations

657 For the semiclassical analysis, we will utilize a mixed basis representation of the quantizations  
658 as in [59, 62, 63]. The generic quantization Eq. (4) is written in the position basis, acting on  
659 position states  $|n\rangle$  and returning states expressed in the position basis. To express a position  
660 basis quantization  $\hat{U}_{N,\text{pos}}$  in the momentum basis, one takes  $\hat{U}_{N,\text{mom}} = \hat{F}_N^{\theta_1, \theta_2} \hat{U}_{N,\text{pos}} (\hat{F}_N^{\theta_1, \theta_2})^{-1}$ .  
661 For the *mixed* basis quantization, one takes  $\hat{U}_{N,\text{mix}} = \hat{F}_N^{\theta_1, \theta_2} \hat{U}_{N,\text{pos}}$ , which now acts on position  
662 states  $|n\rangle$  on the right and momentum dual states  $\langle k|$  on the left. Due to the structure of all  
663 the quantizations we consider, the mixed basis quantization has a simple block DFT structure.  
664 In what follows, quantizations with the subscript “mix” will denote the representation in the  
665 mixed basis.

666 The generic quantization Eq. (4) of the  $A$ -baker’s map  $B$  has the simple block diagonal  
667 mixed basis representation,

$$\hat{U}_{N,\text{mix}}(\alpha) = \bigoplus_{j=0}^{A-1} e^{2\pi i \alpha_j} \hat{F}_{N/A}^{\theta_1, \theta_2}.$$

668 The classical  $t$ -step  $A$ -baker’s map  $B^t$  can be quantized in a similar way. Letting  $\nu_n = \lfloor A^t n/N \rfloor$ ,  
669 which identifies the length  $t$   $A$ -ary string corresponding to  $n/N$ , the corresponding quantiza-  
670 tion for  $B^t$  is, in mixed basis,

$$\langle k | \hat{U}_{\text{mix}}^{(t)}(\alpha) | n \rangle = \delta_{\nu_n, \bar{\nu}_k} \langle k - \bar{\nu}_n N/A^t | \hat{F}_{N/A^t}^{\theta_1, \theta_2} | n - \nu_n N/A^t \rangle e^{2\pi i \sum_{j=0}^{A-1} \alpha_j \eta_j(\nu_n)}, \quad (32)$$

671 where  $\eta_j(\nu)$  denotes the number of  $j$ ’s in the base  $A$  expansion of  $\nu$ . The  $\delta_{\nu_n, \bar{\nu}_k}$  term specifies  
672 where to place the DFT block  $\hat{F}_{N/A^t}^{\theta_1, \theta_2}$ ; it places it in the row  $k$  corresponding to the classical  
673  $A$ -baker’s map image of the rectangle  $[\nu_n/A^t] \times [0, 1]$ , where  $[\nu_n/A^t]$  denotes the interval  
674  $[\frac{\nu_n}{A^t}, \frac{\nu_n+1}{A^t})$ . One can verify Eq. (32) has the correct phase factor involving  $\alpha$  by comparing the  
675 action on coherent states to that of  $\hat{U}_N(\alpha)^t$ . A phase  $e^{2\pi i \alpha_j}$  is accumulated for every  $j$  in  $\nu$ ,  
676 since a current  $q$  value of  $0.a \cdots$  (written in base  $A$ ) corresponds to choosing the  $a$ th DFT block.

677 The  $t$ -step quantization in Eq. (32) is not identical to the 1-step quantization  $\hat{U}_N(\alpha)$  com-  
678 posed  $t$  times, but it is an approximation useful for deriving analytical expressions using a  
679 periodic orbit expansion [62, 63]. We will refer to the quantization Eq. (32) of the  $t$ -step map  
680 as the  $(t)$ -step propagator, with parenthesis, to distinguish it from the 1-step quantization com-  
681 posed  $t$  times. Using Eq. (32) (with Eq. (D.2)) for the  $(t)$ -step propagator in the saddle point  
682 method described in [63, §4] yields the approximation for  $N \rightarrow \infty$ ,

$$\text{tr } \hat{U}^{(t)} \approx \sum_{\nu=0}^{A^t-1} \frac{A^{t/2}}{A^t-1} e^{2\pi i N S_\nu} \exp\left(2\pi i \sum_{j=0}^{A-1} \alpha_j \eta_j(\nu)\right). \quad (33)$$

683 As we assume  $t \rightarrow \infty$  (though slowly) in  $N$ , we can replace  $\frac{A^{t/2}}{A^t-1}$  by  $\frac{1}{A^{t/2}}$ . Each value  $\nu$  in the  
684 sum in Eq. (33) corresponds to a length  $t$  periodic orbit, given by the coordinates  $\nu = a_1 \dots a_t$   
685 in base  $A$ .

686 To estimate the SFF  $\frac{1}{N} |\text{tr } \hat{U}^{(t)}|^2$ , we expand Eq. (33) in a double sum over indices  $\nu, \sigma$ .  
687 Because of the large factor  $N$  in the resulting term  $e^{2\pi i N(S_\nu - S_\sigma)}$ , we ignore any pairs  $(\nu, \sigma)$

688 with  $S_\nu \neq S_\sigma$ , since they are likely to average out due to the rapid oscillations. This the  
 689 “diagonal approximation” method in periodic orbit theory [9]. We know that  $S_\nu = S_\sigma$  for  
 690  $\sigma \in \{\nu, \bar{\nu}, R(\nu), R(\bar{\nu})\}$ , and also for any  $\sigma$  that is a rotation of any of the four above elements.  
 691 (A periodic orbit  $\nu = a_1 \cdots a_t$  is equivalent to the rotated orbit  $a_2 \cdots a_t a_1$ , and so on.) For  
 692 most  $\nu$ , there are thus  $4t$  choices of  $\sigma$  that we know satisfy  $S_\nu = S_\sigma$ . We have overcounted  
 693 for some  $\nu$  however, in particular for the  $\nu$  that are repetitions of a shorter sequence, or  $\nu$   
 694 for which  $\{\nu, \bar{\nu}, R(\nu), R(\bar{\nu})\}$  contains duplicates. However, we can count that there are only of  
 695 order  $\mathcal{O}(A^{t/2})$  such  $\nu$ , which is exponentially small compared to the total number  $A^t$  for large  
 696  $t$ . Therefore in what follows we can ignore the differences for such  $\nu$  since they contribute  
 697 non-leading order terms.

698 Assuming the above-described  $4t$  values for  $\sigma$  are usually or on average the only main  
 699 orbits with  $S_\sigma = S_\nu$ , the diagonal approximation (with the symmetries) then yields

$$\begin{aligned} \frac{1}{N} |\text{tr} \hat{U}^{(t)}|^2 &\approx \sum_{\nu=0}^{A^t-1} \frac{t}{NA^t} \left( 2 + 2e^{2\pi i \sum_{j=0}^{A-1} \alpha_j [\eta_j(\nu) - \eta_j(R(\nu))]} \right) \\ &= \frac{2t}{N} + \frac{2t}{NA^t} \sum_{\nu=0}^{A^t-1} e^{2\pi i \sum_{j=0}^{A-1} \eta_j(\nu)(\alpha_j - \alpha_{A-1-j})} \\ &= \frac{2t}{N} + \frac{2t}{NA^t} \left( \sum_{j=0}^{A-1} \exp(2\pi i(\alpha_j - \alpha_{A-1-j})) \right)^t, \end{aligned} \quad (34)$$

700 where we used the multinomial expansion to obtain the last line, since

$$\sum_{\nu=0}^{A^t-1} \exp\left(2\pi i \sum_{j=0}^{A-1} \eta_j(\nu)(\alpha_j - \alpha_{A-1-j})\right) = \sum_{\substack{n_0 + \dots + n_{A-1} = t \\ n_j \in \mathbb{N}_0}} \binom{t}{n_0, \dots, n_{A-1}} \prod_{j=0}^{A-1} (e^{2\pi i(\alpha_j - \alpha_{A-1-j})})^{n_j}.$$

701 In order for the second term of Eq. (34) not to decay against the  $A^t$  term in the denominator  
 702 as  $t \rightarrow \infty$ , we must have  $\alpha_j - \alpha_{A-1-j} = c \pmod{1}$  for a constant  $c$  and all  $j = 0, \dots, A-1$ , which  
 703 requires  $c = 0$  or  $1/2 \pmod{1}$  by considering  $j = k$  and  $j = A-1-k$ . In the case  $c = 0$ , we  
 704 obtain  $\frac{1}{N} |\text{tr} \hat{U}^{(t)}|^2 \approx \frac{4t}{N}$ , giving an SFF slope of 4 at zero. In the latter case  $c = 1/2$ , we obtain  
 705  $\frac{1}{N} |\text{tr} \hat{U}^{(t)}|^2 \approx \frac{2t}{N} (1 + (-1)^t)$ , giving an average SFF slope (averaged over  $t$ ) of 2 at zero. Thus  
 706 as stated in Sec. 3, we only obtain an SFF slope of 4 if  $\alpha_j = \alpha_{A-1-j}$  for all  $j$ , and obtain a slope  
 707 of 2 in all other cases.

### 708 6.3 Periodic orbit theory for the Shor baker quantizations

709 Recall the arbitrary phase version of the Shor baker matrices was defined in Tab. 1 as

$$\hat{U}_N(\alpha) = \hat{F}_N^{-1} \left( \bigoplus_{j=0}^{A-1} e^{2\pi i \alpha_j} \hat{F}_{N/A}^{0, -j/A} \right). \quad (35)$$

710 In order to estimate the SFF using the periodic orbit expansion, we must identify the cor-  
 711 rect  $t$ -step quantization  $\hat{U}^{(t)}$  corresponding to  $\hat{U}_N(\alpha)$ . For simplicity, we first take all block  
 712 phases  $\alpha_j = 0$ , since they can be added in at the end. We next need to keep track of the  
 713 phases of the 1-step propagator, which we do by calculating its action on maximally localized  
 714 Gaussian-like states (coherent states)  $\Psi_{(q_0, p_0), \sigma, \mathbb{T}^2}$  as defined on the torus, see e.g. [39, 71, 72].  
 715 For  $j \in \{0, 1, \dots, A-1\}$ , let  $\frac{j}{A} \leq q < \frac{j+1}{A}$ , and also assume  $q$  is far enough away from the  
 716 boundaries  $\frac{1}{A}\mathbb{Z}$  to avoid diffraction effects near the classical map’s discontinuities. Following

717 the calculations in [39, Suppl. Mat. §III], then for

$$\tilde{U}_N := \bigoplus_{j=0}^{A-1} \hat{F}_{N/A}^{0, \beta_j}$$

718 and  $\Psi_{(q_0, p_0), \sigma, \mathbb{T}^2}$  the torus coherent state at  $(q_0, p_0)$ , we have the evolution

$$\tilde{U}_N \Psi_{(q_0, p_0), \sigma, \mathbb{T}^2} = e^{i\pi N j q_0} e^{i\pi N j(p_0+j)/A} e^{-2\pi i \beta_j p_0} \Psi_{(Aq_0-j, \frac{p_0+j}{A}), \frac{\sigma}{A^2}, \mathbb{T}^2} + o(1), \quad (36)$$

719 with the error term  $o(1)$  as  $N \rightarrow \infty$ , which includes error from an  $\mathcal{O}(N^{-1})$  shift in the co-  
720 herent state center. The phase  $e^{-2\pi i \beta_j p_0}$  is the extra phase due to the  $\beta_j$ . Starting with a  $q_0$   
721 corresponding to  $\nu = a_1 \cdots a_t$ , then after  $t$  applications of  $\hat{S}_N$ , we accumulate the phase (due  
722 to the  $\beta_j$ )

$$\exp\left(-2\pi i \sum_{j=1}^{t-1} \beta_{a_j} \left[ \sum_{i=1}^{j-1} \frac{a_i}{A^{j-i}} + \frac{p_0}{A^{j-1}} \right]\right). \quad (37)$$

723 The expression in hard brackets  $[\cdots]$  is the momentum coordinate just before applying the  
724  $j$ th iteration. If we write  $p_0 = 0.b_1 b_2 \dots$  in base  $A$ , then at this step the classical infinite binary  
725 sequence is  $\cdots b_2 b_1 a_1 \cdots a_{j-1} \bullet a_j \cdots a_t \cdots$ , which corresponds to the aforementioned phase.  
726 Taking  $\beta_j = -j/A$ , then Eq. (37) becomes

$$\exp\left(2\pi i \sum_{j=1}^{t-1} a_j \sum_{i=1}^{j-1} \frac{a_i}{A^{j-i+1}}\right) e^{2\pi i \nu p_0 / A^t}. \quad (38)$$

727 Next we assume the  $t$ -step propagator  $\hat{U}^{(t)}$  is of the form  $\hat{F}_N^{-1} \hat{U}_{\text{mix}}^{(t)}$  with  $\langle k | \hat{U}_{\text{mix}}^{(t)} | n \rangle = \delta_{\nu_n \bar{\nu}_k} \hat{F}_{N/A^t}^{0, b(\nu)} e^{-2\pi i \psi(\nu)}$   
728 for some  $b(\nu)$  and  $\psi(\nu)$ . As in Eq. (36), the  $b(\nu)$  term will produce an extra phase  $e^{-2\pi i b(\nu) p_0}$ .  
729 Comparing this to Eq. (38) leads to the relations  $b(\nu) = -\nu/A^t$  and  $\psi(\nu) = \phi(\nu)/A$ . Adding  
730 in the  $\alpha_j$  phases then yields the  $(t)$ -step propagator for Eq. (35) in mixed basis as

$$\langle k | \hat{U}_{\text{mix}}^{(t)}(\alpha) | n \rangle = \delta_{\nu_n \bar{\nu}_k} \hat{F}_{N/A^t}^{0, -\nu/A^t} e^{-2\pi i \phi(\nu)/A} e^{2\pi i \sum_{j=0}^{A-1} \alpha_j \eta_j(\nu_n)}, \quad (39)$$

731 where

$$\phi(\nu) = -\sum_{j=2}^t a_j \sum_{i=1}^{j-1} a_i A^{-j+i}. \quad (40)$$

732 For visualization purposes, we include graphics below in the style of [59] (which plotted  $t$ -  
733 step propagators for the Saraceno quantization) to visually demonstrate Eq. (39) for the Shor  
734 baker quantization with  $A = 2$ . This involves comparing  $\hat{U}_{\text{mix}}^{(t)}$  to the mixed basis propagator  
735  $\hat{S}_{N, \text{mix}}^t := \hat{F}_N \hat{S}_N^t$ , where

$$\hat{S}_N = \hat{F}_N^{-1} \begin{pmatrix} \hat{F}_{N/2} & \\ & -\hat{F}_{N/2}^{0, -1/2} \end{pmatrix},$$

736 is the usual  $A = 2$  Shor baker quantization. In Figs. 12 and 13, for  $t = 2$  and 3, we plot the  
737 mixed basis matrix entry sizes and phases of  $\hat{S}_N^t$ , and observe close agreement with those of  
738 the  $(t)$ -step propagator  $\hat{U}_{\text{mix}}^{(t)}$  from Eq. (39) for  $A = 2$ .

739 With the stationary phase approximation (see Appendix D for details), Eq. (39) leads to

$$\text{tr} \hat{U}^{(t)} \approx \sum_{\nu=0}^{A^t-1} \frac{1}{A^{t/2}} e^{2\pi i N S_\nu} e^{\frac{2\pi i \nu \bar{\nu}}{A^t(A^t-1)}} e^{-2\pi i \frac{\phi(\nu)}{A}} e^{2\pi i \sum_{j=0}^{A-1} \alpha_j \eta_j(\nu)}. \quad (41)$$



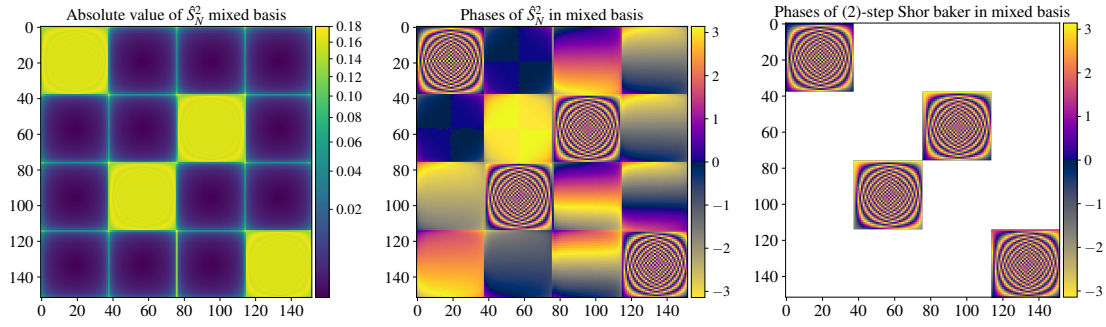


Figure 12: Visual example for Eq. (39). (Left) Plot of the matrix entry sizes of  $\hat{S}_{N,\text{mix}}^2$  for  $N = 152$ . The non-DFT-like blocks have much smaller matrix elements, other than possibly at the block boundary lines. (Center) Phase plot of the entries of  $\hat{S}_{N,\text{mix}}^2$ . Note the different color patterns in each generalized DFT block (most evident by looking at the four corner areas of each block). This corresponds to different generalized DFT phases and different block phases. (Right) Phase plot of the (2)-step propagator in Eq. (39) with  $\alpha = 0$ . By carefully considering the different color patterns, one can see they match those of the center plot for  $\hat{S}_{N,\text{mix}}^2$ .

740 From Eq. (40), one can check that  $\phi(\nu) = \phi(\bar{\nu})$ , and that

$$\phi(R(\nu)) = \phi(\nu) - (A-1)t + A - \frac{1}{A^{t-1}} + 2 \sum_{i=1}^t a_i - \frac{\nu + \bar{\nu}}{A^{t-1}}.$$

741 Then we obtain

$$\frac{\nu \bar{\nu}}{A^t(A^t - 1)} - \frac{\phi(\nu)}{A} - \left( \frac{R(\nu)R(\bar{\nu})}{A^t(A^t - 1)} - \frac{\phi(R(\nu))}{A} \right) = - \left( 1 - \frac{1}{A} \right) t + \frac{2}{A} \sum_{i=1}^t a_i. \quad (42)$$

742 Additionally, if  $\nu' = a_2 \cdots a_t a_1$  is the 1-step cyclic rotation of  $\nu = a_1 \cdots a_t$ , then calculation  
743 shows that

$$\frac{\phi(\nu')}{A} = \frac{\phi(\nu)}{A} + \frac{a_1}{A^t}(\nu - \bar{\nu}'),$$

744 so that also using  $\frac{\nu' \bar{\nu}'}{A^{t-1}} = \frac{\nu \bar{\nu}}{A^{t-1}} + a_1(\nu - \bar{\nu}')$ , we obtain

$$\frac{\nu \bar{\nu}}{A^t(A^t - 1)} - \frac{\phi(\nu)}{A} = \frac{\nu' \bar{\nu}'}{A^t(A^t - 1)} - \frac{\phi(\nu')}{A}. \quad (43)$$

745 Then taking the diagonal approximation (with symmetry factors) to only sum over  $\sigma \in \{\nu, \bar{\nu}, R(\nu), R(\bar{\nu})\}$   
746 and their cyclic rotations, yields similarly to Eq. (34),

$$\begin{aligned} \frac{1}{N} |\text{tr} \hat{U}^{(t)}|^2 &\approx \frac{t}{NA^t} \sum_{\nu=0}^{A^t-1} \left( 2 + 2 \exp \left( 2\pi i \sum_{j=0}^{A-1} \alpha_j [\eta_j(\nu) - \eta_j(R(\nu))] \right) e^{2\pi i [-(1-\frac{1}{A})t + \frac{2}{A} \sum_{i=1}^t a_i]} \right) \\ &= \frac{2t}{N} + \frac{t}{NA^t} \sum_{\nu=0}^{A^t-1} 2 \exp \left( 2\pi i \sum_{j=0}^{A-1} \eta_j(\nu) \left( \alpha_j - \alpha_{A-1-j} + \frac{2j}{A} \right) \right) e^{-2\pi i (1-\frac{1}{A})t} \\ &= \frac{2t}{N} + \frac{2t}{NA^t} \left( \sum_{j=0}^{A-1} \exp \left( 2\pi i (\alpha_j - \alpha_{A-1-j} + 2j/A) \right) \right)^t e^{2\pi i t/A}. \end{aligned} \quad (44)$$

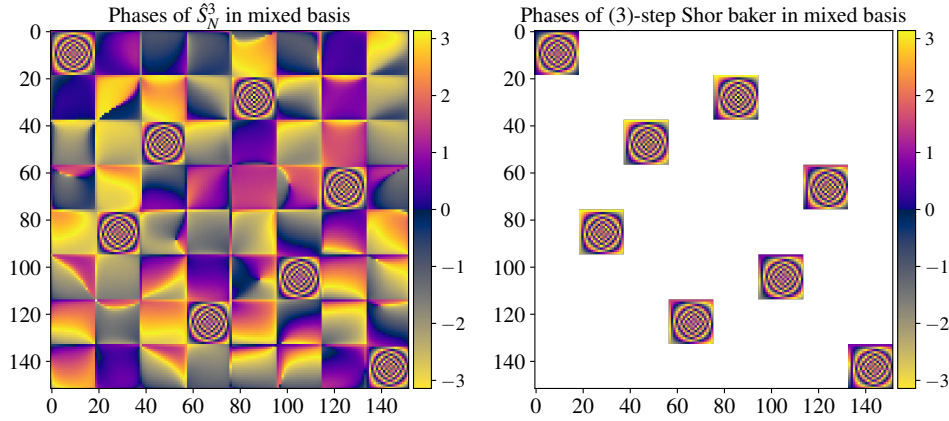


Figure 13: Phase plot equivalents of Fig. 12 for  $t = 3$ . As in the  $t = 2$  case, note the careful agreement between the phases of  $\hat{S}_{N,\text{mix}}^3$  and those of the (3)-step propagator from Eq. (39).

747 In order to have non-decaying second term as  $t \rightarrow \infty$ , we need (modulo 1)

$$\alpha_j - \alpha_{A-1-j} + \frac{2j}{A} = c, \quad \forall j = 0, \dots, A-1.$$

748 By considering  $j = k$  and  $j = A-1-k$ , we must have  $c = -\frac{1}{A}$  or  $-\frac{1}{A} + \frac{1}{2}$  (mod 1). In the former,  
 749 Eq. (44) becomes  $\frac{4t}{N}$ , while in the latter it becomes  $\frac{2t}{N}(1 + (-1)^t)$  which averages to slope 2.  
 750 Thus we obtain an averaged SFF slope of 4 iff

$$\alpha_{A-1-j} = \alpha_j + \frac{2j+1}{A} \pmod{1}, \quad j = 0, \dots, A-1, \quad (45)$$

751 and slope 2 in all other cases.

## 752 7 Conclusion

753 We have studied maximally chaotic quantum maps with discrete symmetries that share the  
 754 same classical limit. Contrary to conventional expectations for the correspondence between  
 755 discrete symmetries and spectral statistics [10, 45–48], we demonstrated that short-range spec-  
 756 tral statistics in these models generically fail to identify discrete symmetries (weak anomalies),  
 757 while long-range spectral statistics also violate these expectations in the presence of phases  
 758 (strong anomalies). However, long-range spectral statistics appear more directly correlated  
 759 with intrinsic quantum dynamical properties [27] in the Hilbert space. This further reinforces  
 760 the notion that spectral statistics should ideally be interpreted in terms of intrinsically quan-  
 761 tum mechanical properties, while more work is necessary to understand how they connect to  
 762 macroscopic dynamics, such as in the classical limit, beyond the well-studied case of systems  
 763 showing close agreement in several measures with RMT [1, 3].

764 One direction to explore, which may be of immediate relevance in the context of many-  
 765 body statistical mechanics, is whether the introduction of simple phases — as in the case of  
 766 strong anomalies studied here — could break the commonly observed correspondence [2, 22]  
 767 between “macroscopic” subsystem thermalization behaviors (i.e. in a large subset of particles)  
 768 and spectral signatures of ergodic phenomena. While our results already formally point to  
 769 an affirmative answer, given that one can realize quantizations of  $A$ -baker’s maps as many-  
 770 body Floquet quantum circuits using the quantum Fourier transform and phase gates [52, 53]

771 (with the classical  $N \rightarrow \infty$  limit then corresponding to the thermodynamic limit of, e.g., many  
 772 qubits), it would nevertheless be illuminating to understand the mechanisms involved (such  
 773 as Berry-like phases) in a more natural setting of an interacting many-body system that does  
 774 not necessarily model a classically chaotic map.

## 775 Acknowledgements

776 This work was supported by the U.S. Department of Energy, Office of Science, Basic Energy Sci-  
 777 ences under Award No. DE-SC0001911 and the Simons Foundation. The authors acknowledge  
 778 the University of Maryland supercomputing resources (<https://hpcc.umd.edu>) made available  
 779 for conducting the research reported in this paper. We thank Abu Musa Patoary for useful dis-  
 780 cussions.

## 781 A Reflection commutators

782 In this section, we provide numerical evidence that the (generic) generic quasiperiodic and  
 783 Shor baker quantizations do not have a Fourier reflection symmetry, as defined below. We also  
 784 provide numerical plots demonstrating symmetries of various eigenvectors.

785 We will say that a quantization  $\hat{U}_N$  has a “Fourier reflection symmetry” if  $\hat{U}_N$  commutes  
 786 with some  $\tilde{R}_N^{\omega_1, \omega_2} := (\hat{F}_N^{\omega_1, \omega_2})^2$ , for  $(\omega_1, \omega_2) \in [0, 1]^2$ , for each  $N \in \mathbb{AN}$ . Interestingly enough,  
 787 there is a generic quantization  $\text{Gen}_{A=2}^{0.5, 0}$  that does not commute with its “natural” reflection  
 788 candidate  $\tilde{R}_N^{0.5, 0}$ , but does commute with  $\tilde{R}_N^{0, 0}$ , and so counts as possessing a Fourier reflection  
 789 symmetry. As discussed in Sec. 4.1, these Fourier reflection symmetries are only a small subset  
 790 of all possible quantum reflection operators.

791 Letting  $\hat{B}_{A,N}^{\theta_1, \theta_2}$  be the generic quasiperiodic quantization for the  $A$ -baker’s map, we plot the  
 792 Frobenius matrix norm for a variety of commutators  $[\hat{B}_{N,A}^{\theta_1, \theta_2}, \tilde{R}_N^{\omega_1, \omega_2}]$  in Fig. 14. It appears that  
 793 the Balazs–Voros quantization, most generic quasiperiodic quantizations, and the Shor baker  
 794 quantization have nonzero commutators and do not possess a Fourier reflection symmetry.

795 In Fig. 16, we plot the Husimi functions of eigenstates of the various quantizations. The  
 796 Husimi function is a phase space representation of a vector  $v \in \mathbb{C}^N$ , defined using the overlap  
 797 with coherent states. For a precise definition and further background, see [73]. This type of  
 798 phase space representation was used in [50] to study scarring of the eigenstates of the Sara-  
 799 ceno quantization. Depending on the quantization, the eigenstates may or may not preserve  
 800 the classical reflection or TR symmetries, which can suggest information about possible quan-  
 801 tum symmetries. However, we emphasize that Fig. 16 provides only a rough visual indication  
 802 of symmetries, of only a select sample of eigenstates, and moreover may contain finite-size  
 803 effects. Therefore, while the Husimi functions exhibit different symmetries depending on the  
 804 quantization, they can provide interesting but not conclusive evidence about quantum ana-  
 805 logues of the classical symmetries.

## 806 B Commutator for approximate symmetry

807 In this section, we analytically check the approximate symmetry  $\tilde{R}_N$  introduced in Section 4.3  
 808 (Eq. (25)) is in some sense close to commuting with the Balazs–Voros quantization  $\hat{B}_{N,A}$ . More  
 809 precisely, for  $\hat{B}_{N,A}$  the Balazs–Voros quantization and  $\tilde{R}_N = \tilde{R}_N^{0, 0}$ , we show the only possible  
 810 large matrix elements  $\langle x | [\hat{B}_{N,A}, \tilde{R}_N] | y \rangle$  of the commutator  $[\hat{B}_{N,A}, \tilde{R}_N]$  are those  $(x, y)$  with

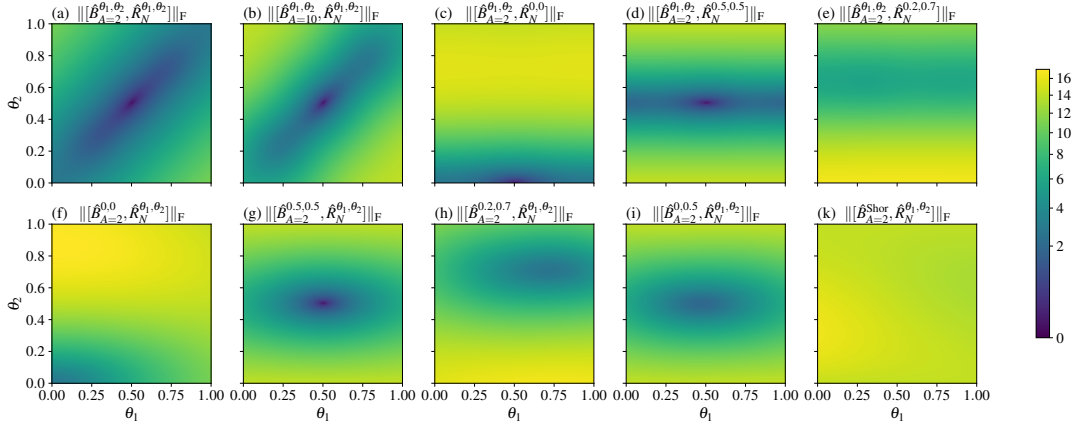


Figure 14: (a)–(e): Plots of the Frobenius matrix norm of the commutator  $[\hat{B}_{N,A}^{\theta_1, \theta_2}, \tilde{R}_N^{\omega_1, \omega_2}]$  as a function of  $\theta = (\theta_1, \theta_2)$ , for: (a)–(b)  $\omega = \theta$ , (c)  $\omega = (0, 0)$ , (d)  $\omega = (0.5, 0.5)$ , and (e)  $\omega = (0.2, 0.7)$ . In all cases  $N = 100$ . In (a), (b), and (d), the commutator is zero only at  $\theta_1 = \theta_2 = 1/2$ , which corresponds to the Saraceno quantization. In (c), the  $\text{Gen}_{A=2}^{0.5, 0}$  quantization is seen (perhaps surprisingly) to commute with  $\hat{R}_N^{0, 0}$ . However, in (e) and for randomly chosen  $\omega$ , it appears that  $\|[\hat{B}_{N,A}^{\theta_1, \theta_2}, \tilde{R}_N^{\omega_1, \omega_2}]\|_F$  is bounded away from zero for all  $\theta$ . (f)–(k): Plots of the Frobenius matrix norm of the commutator  $[\hat{U}_N, \tilde{R}_N^{\theta_1, \theta_2}]$ , where  $\hat{U}_N$  is a fixed quantization and  $\tilde{R}_N^{\theta_1, \theta_2}$  ranges over  $\theta \in [0, 1]^2$ . In all plots except for the Saraceno quantization in (g), the matrix norm appears bounded away from zero, indicating the quantizations should not have a Fourier reflection symmetry. Plots for  $A = 10$  appear similar, and plots for the phase variant quantizations also appear bounded away from zero. In all of the above plots, the sampling mesh is size  $200 \times 200$ .

811  $y \in \frac{N}{A}\mathbb{Z}$  and with  $x$  close to 0 or  $N$  and not in  $A\mathbb{Z}$ .

812 Let  $a, b \in \{0, \dots, A-1\}$  be defined so that  $a\frac{N}{A} \leq y < (a+1)\frac{N}{A}$  and  $b\frac{N}{A} \leq N-y \pmod{N} < (b+1)\frac{N}{A}$ .

813 Using that  $\tilde{R}_N|y\rangle = |N-y\rangle$  (taken modulo  $N$ ), direct evaluation shows,

$$\langle x | [\hat{B}_{N,A}, \tilde{R}_N] | y \rangle = \frac{\sqrt{A}}{N} \sum_{m=0}^{N/A-1} \left[ e^{2\pi i a x/A} e^{2\pi i x m/N} e^{2\pi i m y A/N} - e^{2\pi i x b/A} e^{-2\pi i x m/N} e^{-2\pi i m y A/N} \right]. \quad (\text{B.1})$$

814 First, if  $x + yA \in N\mathbb{Z}$ , which would prevent geometric summation, then since  $A|N$  we must also  
 815 have  $x \in A\mathbb{Z}$ . Combined with  $x + yA \in N\mathbb{Z}$ , then Eq. (B.1) is zero in this case. For  $x + yA \notin N\mathbb{Z}$ ,  
 816 we can evaluate,

$$\langle x | [\hat{B}_{N,A}, \tilde{R}_N] | y \rangle = \frac{\sqrt{A}}{N} \left[ e^{2\pi i a x/A} \frac{e^{2\pi i x/A} - 1}{e^{2\pi i x/N} e^{2\pi i y A/N} - 1} - e^{-2\pi i b x/A} \frac{e^{-2\pi i x/A} - 1}{e^{-2\pi i x/N} e^{-2\pi i y A/N} - 1} \right], \quad (\text{B.2})$$

817 which we see is zero if  $x \in A\mathbb{Z}$ . If  $y \in \frac{N}{A}\mathbb{Z}$ , then one can check that  $a + b \in \{0, A\}$ , and we use  
 818 the bound  $|e^{2\pi i x/N} e^{2\pi i y A/N} - 1| \geq \frac{c}{N} d(x, N\mathbb{Z})$  for a numerical constant  $c > 0$ . This gives the  
 819 bound

$$\langle x | [\hat{B}_{N,A}, \tilde{R}_N] | y \rangle = \mathcal{O}\left(\frac{\sqrt{A}}{d(x, N\mathbb{Z})}\right), \quad (\text{B.3})$$

820 which thus allows large commutator matrix elements for the  $A$  values of  $y \in \frac{N}{A}\mathbb{Z} \cap [0, N-1]$   
 821 and  $x$  close to 0 or  $N$  (and not in  $A\mathbb{Z}$ ).

822 If  $y \notin \frac{N}{A}\mathbb{Z}$ , then one can check  $a + b = A - 1$ , and we obtain from Eq. (B.2) that

$$\langle x | [\hat{B}_{N,A}, \tilde{R}_N] | y \rangle = \frac{\sqrt{A}}{N} e^{2\pi i a x/A} (1 - e^{2\pi i x/A}) = \mathcal{O}\left(\frac{\sqrt{A}}{N}\right),$$

823 which is small. Thus the only possible large matrix elements of the commutator  $[\hat{B}_{N,A}, \tilde{R}_N]$  are  
 824 those  $(x, y)$  from Eq. (B.3) with  $y \in \frac{N}{A}\mathbb{Z}$  and  $x$  close to 0 or  $N$  and not in  $A\mathbb{Z}$ .

## 825 C Details for the computation of the early time SFF slope

826 In this section, we provide the details for our numerical computations of the early time SFF  
 827 slope. Examples of RMT behavior and (rare) bad early time behavior are shown in Fig. 15.

- 828 1. We averaged the SFF at time  $t$  with its nearest  $2\ell$  neighbors (or up to time  $2t - 1$  if  
 829  $t < \ell$ ), with  $\ell = 20$  for  $N < 1000$  and  $\ell = 40$  for  $N \geq 1000$ . The choice of averaging to  
 830 time  $2t - 1$  for  $t < \ell$  keeps the averaging symmetric about  $t$ .
- 831 2. We took the first  $f$  points of the above averaged SFF, where  $f = 20$  for  $N < 1000$ ,  
 832  $f = 40$  for  $1000 \leq N < 5000$ , and  $f = 60$  for  $N \geq 5000$ , and ran a least squares fit  
 833 for a line through the origin to get the best slope. We also retained the scaled residual  
 834 error, which is the residual error when running the least squares fit for  $x \in [1 : f]$  and  
 835  $y = N \text{ SFF}(x)$ .
- 836 3. We removed all ‘‘outliers’’ which had scaled residual error over 100 (or 400 for  $A = 15$ ,  
 837 to make sure not too many points were removed). We then averaged the slopes among  
 838 points within 10 units away (ignoring outliers) and plotted the resulting slopes. We note  
 839 that the removed outlier points are not necessarily those with an outlier SFF slope value,  
 840 but just those for which the least squares fit did not work well.

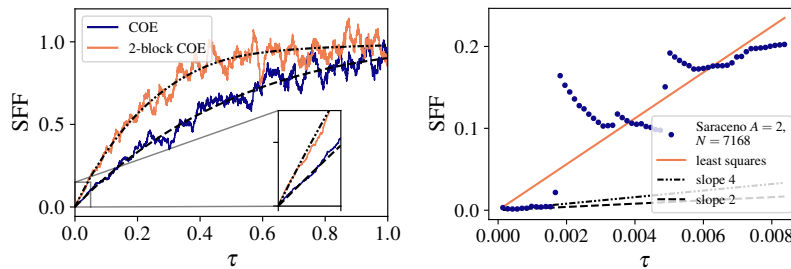


Figure 15: (Left) SFF for random instances of a COE and a 2-block COE matrix for reference, with  $N = 9690$  and  $\ell = 100$ . There is a clear distinction between COE and 2-block COE with this averaging method, which in particular identifies the slope near 0. (Right) Example of the least squares fit for a removed outlier of the Saraceno  $A = 2$  quantization,  $N = 7168$  (plotted for longer times in Fig. 11(b)). Removed outliers amount to only 0.86% of the values of  $N \in 2\mathbb{N}$  considered for this quantization in Fig. 10(b).

## 841 D Shor baker matrix stationary phase approximation

842 We provide more details for adapting the saddle point method from [63] to the Shor baker  
 843 quantizations, which we recall involve several different generalized DFT blocks. The resulting



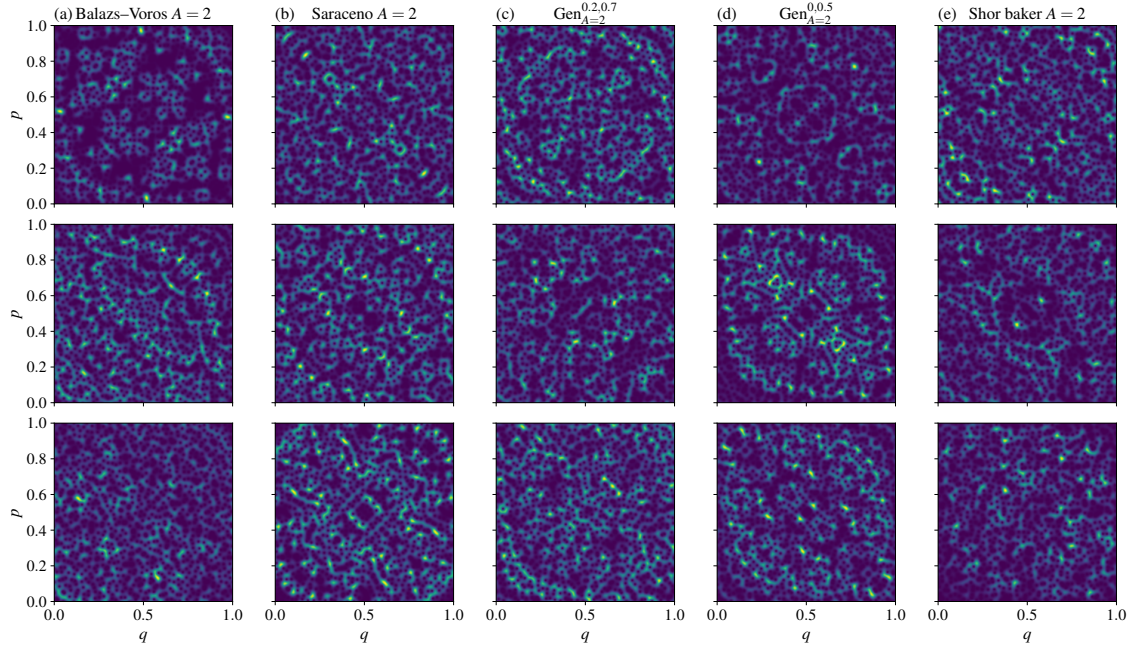


Figure 16: Husimi (phase space) plots for eigenvectors of the various quantizations for  $N = 1000$  and mesh size  $300 \times 300$ , arranged by column. A reflection symmetry across the line  $p = q$  corresponds to the classical TR symmetry  $(q, p) \mapsto (p, q)$ , while a reflection symmetry across the line  $p = 1 - q$  corresponds to the classical reflection symmetry  $(q, p) \mapsto (1 - q, 1 - p)$ . While all quantizations have some eigenvectors that appear to preserve both symmetries (top row), it appears the quantizations that do not have a clear quantum analogue of the classical symmetries can have eigenvectors that break a symmetry (middle and bottom rows of columns (a), (c), and (e)). Of the eigenvectors sampled for the  $\text{Gen}_{A=2}^{0.0,0.5}$  quantization in column (d), however, they appear to generally preserve both classical symmetries.

844 extra phase factors in Eq. (D.1) below will be important for the analysis. We start with the  
 845  $t$ -step quantization  $\hat{U}_{\text{mix}}^{(t)}$  in Eq. (39), for simplicity with block phases  $\alpha_j = 0$  since they can  
 846 be added in later. The nonzero blocks in  $\hat{U}_{\text{mix}}^{(t)}$  correspond to coordinates  $(n, k)$  with  $\nu_n = \bar{\nu}_k$ .  
 847 Equivalently, picking a  $\nu$ , then there is the block where  $\frac{N\nu}{A^t} \leq n < \frac{N(\nu+1)}{A^t}$  and  $\frac{N\bar{\nu}}{A^t} \leq k < \frac{N(\bar{\nu}+1)}{A^t}$ .  
 848 For these coordinates,

$$\begin{aligned} \langle k | \hat{U}_{\text{mix}}^{(t)} | n \rangle &= \langle k - \bar{\nu}N/A^t | \hat{F}_{N/A^t}^{0, -\frac{\nu}{A^t}} | n - \nu N/A^t \rangle e^{-2\pi i \phi(\nu)/A} \\ &= \langle k - \bar{\nu}N/A^t | \hat{F}_{N/A^t}^{0,0} | n - \nu N/A^t \rangle e^{2\pi i k \nu / N} e^{-2\pi i \nu \bar{\nu} / A^t} e^{-2\pi i \phi(\nu)/A}. \end{aligned} \quad (\text{D.1})$$

849 Letting  $F_\nu(q, p) = A^t pq - \nu p - \bar{\nu} q$  be the classical generating function as in [63], there is the  
 850 relation for  $q = (n + \theta_2)/N$  and  $p = (k + \theta_1)/N$ ,

$$\langle k - \bar{\nu}N/A^t | \hat{F}_{N/A^t}^{\theta_1, \theta_2} | n - \nu N/A^t \rangle = \frac{A^{t/2}}{N^{1/2}} e^{-2\pi i N F_\nu(q, p)}. \quad (\text{D.2})$$

851 Since we work with periodic boundary conditions for the Shor baker quantizations, we take  
 852  $\theta_1 = \theta_2 = 0$ . Allowing interpolation to move to continuous coordinates  $q$  and  $p$ , Eq. (D.1)  
 853 then becomes

$$\langle p | \hat{U}_{\text{mix}}^{(t)} | q \rangle \approx \frac{A^{t/2}}{N^{1/2}} e^{-2\pi i N F_\nu(q, p)} e^{2\pi i p \nu} e^{-2\pi i \nu \bar{\nu} / A^t} e^{-2\pi i \phi(\nu)/A}.$$



854 Preparing for the saddle point approximation as in [63, §4] then yields,

$$\begin{aligned}
\text{tr } \hat{U}^{(t)} &= \frac{1}{N^{1/2}} \sum_{k,n=0}^{N-1} e^{2\pi i kn/N} \langle k | U_{\text{mix}}^{(t)} | n \rangle \\
&= \frac{1}{N^{1/2}} \sum_{k,n=-\infty}^{\infty} \int_{-\infty}^{\infty} d(Nq) \int_{-\infty}^{\infty} d(Np) \chi_{[0,1)}(p) \chi_{[0,1)}(q) e^{2\pi i Npq} \langle p | U_{\text{mix}}^{(t)} | q \rangle \times \\
&\hspace{20em} \delta(Nq - n) \delta(Np - k) \\
&\approx N^{3/2} \sum_{\ell,m} \sum_{\nu=0}^{A^t-1} \int_{\frac{\nu}{A^t}}^{\frac{\nu+1}{A^t}} dq \int_{\frac{\bar{\nu}}{A^t}}^{\frac{\bar{\nu}+1}{A^t}} dp e^{2\pi i Npq} e^{-2\pi i m Nq} e^{-2\pi i \ell Np} \frac{A^{t/2}}{N^{1/2}} e^{-2\pi i N F_{\nu}(q,p)} e^{2\pi i p \nu} \times \\
&\hspace{20em} e^{-2\pi i \nu \bar{\nu}/A^t} e^{-2\pi i \phi(\nu)/A} \\
&= NA^{t/2} \sum_{\ell,m} \sum_{\nu=0}^{A^t-1} \int_{\frac{\nu}{A^t}}^{\frac{\nu+1}{A^t}} dq \int_{\frac{\bar{\nu}}{A^t}}^{\frac{\bar{\nu}+1}{A^t}} dp \exp(2\pi i N[pq - A^t pq + (\nu - \ell)p + (\bar{\nu} - m)q]) \times \\
&\hspace{20em} e^{2\pi i p \nu} e^{-2\pi i \nu \bar{\nu}/A^t} e^{-2\pi i \phi(\nu)/A}.
\end{aligned}$$

855 For  $\ell = m = 0$ , the stationary point is  $q = \frac{\nu}{A^t-1}$ ,  $p = \frac{\bar{\nu}}{A^t-1}$ . For other  $(\ell, m)$ , there are no  
856 stationary points in the region of integration, and so ignoring those terms, we thus obtain the  
857 stationary phase estimate

$$\text{tr } \hat{U}^{(t)} \approx \frac{A^{t/2}}{A^t - 1} \sum_{\nu=0}^{A^t-1} e^{2\pi i N S_{\nu}} e^{\frac{2\pi i \nu \bar{\nu}}{A^t(A^t-1)}} e^{-2\pi i \phi(\nu)/A}. \quad (\text{D.3})$$

## 858 References

- 859 [1] F. Haake, S. Gnutzmann and M. Kuś, *Quantum signatures of chaos*, Springer Series in  
860 Synergetics. Springer, Cham, fourth edn., doi:[10.1007/978-3-319-97580-1](https://doi.org/10.1007/978-3-319-97580-1) (2018).
- 861 [2] L. D'Alessio, Y. Kafri, A. Polkovnikov and M. Rigol, *From quantum chaos and eigen-  
862 state thermalization to statistical mechanics and thermodynamics*, Adv. Phys. **65**(3), 239  
863 (2016), doi:[10.1080/00018732.2016.1198134](https://doi.org/10.1080/00018732.2016.1198134).
- 864 [3] M. L. Mehta, *Random matrices*, vol. 142 of *Pure and Applied Mathematics (Amsterdam)*,  
865 Elsevier/Academic Press, Amsterdam, third edn., ISBN 978-0-12-088409-4 (2004).
- 866 [4] S. W. McDonald and A. N. Kaufman, *Spectrum and eigenfunctions for a hamiltonian with  
867 stochastic trajectories*, Phys. Rev. Lett. **42**(18), 1189 (1979).
- 868 [5] G. Casati, F. Valz-Gris and I. Guarneri, *On the connection between quantization of nonin-  
869 tegrable systems and statistical theory of spectra*, Lett. Nuovo Cimento **28**(8), 279 (1980).
- 870 [6] M. V. Berry, *Quantizing a classically ergodic system: Sinai's billiard and the KKR method*,  
871 Ann. Phys. **131**(1), 163 (1981).
- 872 [7] O. Bohigas, M.-J. Giannoni and C. Schmit, *Characterization of chaotic quantum  
873 spectra and universality of level fluctuation laws*, Phys. Rev. Lett. **52**(1), 1 (1984),  
874 doi:[10.1103/PhysRevLett.52.1](https://doi.org/10.1103/PhysRevLett.52.1).
- 875 [8] J. H. Hannay and A. M. Ozorio de Almeida, *Periodic orbits and a correlation function for  
876 the semiclassical density of states*, J. Phys. A **17**(18), 3429 (1984).

- 877 [9] M. V. Berry, *Semiclassical theory of spectral rigidity*, Proc. Roy. Soc. Lond. A **400**(1819),  
878 229 (1985).
- 879 [10] N. Argaman, Y. Imry and U. Smilansky, *Semiclassical analysis of spectral correlations in*  
880 *mesoscopic systems*, Phys. Rev. B **47**(8), 4440 (1993).
- 881 [11] O. Giraud, J. Marklof and S. O’Keefe, *Intermediate statistics in quantum maps*, J. Phys.  
882 A: Math. Gen. **37**(28), L303 (2004).
- 883 [12] Č. Lozej, G. Casati and T. Prosen, *Quantum chaos in triangular billiards*, Phys. Rev. Res.  
884 **4**(1), 013138 (2022), doi:[10.1103/PhysRevResearch.4.013138](https://doi.org/10.1103/PhysRevResearch.4.013138).
- 885 [13] J. Wang, G. Benenti, G. Casati and W.-g. Wang, *Statistical and dynamical properties of the*  
886 *quantum triangle map*, J. Phys. A: Math. Theor **55**, 234002 (2022).
- 887 [14] J. S. Cotler, G. Gur-Ari, M. Hanada, J. Polchinski, P. Saad, S. H. Shenker, D. Stanford,  
888 A. Streicher and M. Tezuka, *Black holes and random matrices*, J. High Energy Phys.  
889 **2017**(5), 1 (2017).
- 890 [15] J. Cotler, N. Hunter-Jones, J. Liu and B. Yoshida, *Chaos, complexity, and random matrices*,  
891 J. High Energy Phys. **2017**(11), 1 (2017).
- 892 [16] P. Kos, M. Ljubotina and T. Prosen, *Many-body quantum chaos: Analytic connection to*  
893 *random matrix theory*, Phys. Rev. X **8**(2), 021062 (2018).
- 894 [17] A. Chan, A. De Luca and J. Chalker, *Solution of a minimal model for many-body quantum*  
895 *chaos*, Phys. Rev. X **8**(4), 041019 (2018).
- 896 [18] B. Bertini, P. Kos and T. Prosen, *Exact spectral form factor in a minimal model of many-body*  
897 *quantum chaos*, Phys. Rev. Lett. **121**(26), 264101 (2018).
- 898 [19] P. Saad, S. H. Shenker and D. Stanford, *A semiclassical ramp in SYK and in gravity*,  
899 preprint arXiv:1806.06840 (2018).
- 900 [20] Y. Liao and V. Galitski, *Universal dephasing mechanism of many-body quantum chaos*,  
901 Phys. Rev. Res. **4**(1), L012037 (2022).
- 902 [21] M. V. Berry and M. Tabor, *Level clustering in the regular spectrum*, Proc. Roy. Soc. Lond.  
903 A **356**, 375 (1977).
- 904 [22] D. A. Abanin, E. Altman, I. Bloch and M. Serbyn, *Colloquium: Many-body localization,*  
905 *thermalization, and entanglement*, Rev. Mod. Phys. **91**(2), 021001 (2019).
- 906 [23] Y. Liao, A. Vikram and V. Galitski, *Many-body level statistics of single-particle quantum*  
907 *chaos*, Phys. Rev. Lett. **125**(25), 250601 (2020).
- 908 [24] M. Winer, S.-K. Jian and B. Swingle, *Exponential ramp in the quadratic Sachdev-Ye-Kitaev*  
909 *model*, Phys. Rev. Lett. **125**(25), 250602 (2020).
- 910 [25] A. Prakash, J. Pixley and M. Kulkarni, *Universal spectral form factor for many-body local-*  
911 *ization*, Phys. Rev. Res. **3**(1), L012019 (2021).
- 912 [26] R. Barney, M. Winer, C. L. Baldwin, B. Swingle and V. Galitski, *Spectral*  
913 *statistics of a minimal quantum glass model*, SciPost Phys. **15**, 084 (2023),  
914 doi:[10.21468/SciPostPhys.15.3.084](https://doi.org/10.21468/SciPostPhys.15.3.084).

- 915 [27] A. Vikram and V. Galitski, *Dynamical quantum ergodicity from energy level statistics*, Phys.  
916 Rev. Res. **5**(3), 033126 (2023).
- 917 [28] J. Hannay and M. V. Berry, *Quantization of linear maps on a torus-fresnel diffraction by*  
918 *a periodic grating*, Phys. D: Nonlinear Phenom. **1**(3), 267 (1980), doi:[10.1016/0167-](https://doi.org/10.1016/0167-2789(80)90026-3)  
919 [2789\(80\)90026-3](https://doi.org/10.1016/0167-2789(80)90026-3).
- 920 [29] J. P. Keating, *The cat maps: quantum mechanics and classical motion*, Nonlinearity **4**(2),  
921 309 (1991).
- 922 [30] P. W. Shor, *Algorithms for quantum computation: discrete logarithms and factoring*, In  
923 *Proceedings 35th annual symposium on foundations of computer science*, pp. 124–134.  
924 IEEE, doi:[10.1109/SFCS.1994.365700](https://doi.org/10.1109/SFCS.1994.365700) (1994).
- 925 [31] E. Bogomolny, U. Gerland and C. Schmit, *Models of intermediate spectral statistics*, Phys.  
926 Rev. E **59**(2), R1315 (1999).
- 927 [32] E. Bogomolny, B. Georgeot, M.-J. Giannoni and C. Schmit, *Arithmetical chaos*, Phys. Rep.  
928 **291**(5–6), 219 (1997), doi:[10.1016/S0370-1573\(97\)00016-1](https://doi.org/10.1016/S0370-1573(97)00016-1).
- 929 [33] W. Luo and P. Sarnak, *Number variance for arithmetic hyperbolic surfaces*, Comm. Math.  
930 Phys. **161**(2), 419 (1994), doi:[10.1007/BF02099785](https://doi.org/10.1007/BF02099785).
- 931 [34] P. Braun and F. Haake, *Level statistics in arithmetical and pseudo-arithmetical chaos*, J.  
932 Phys. A: Math. Theor. **43**(26), 262001 (2010).
- 933 [35] S. Das, S. K. Garg, C. Krishnan and A. Kundu, *What is the simplest linear ramp?*, preprint  
934 arXiv:2308.11704 (2023).
- 935 [36] B. V. Chirikov, F. M. Izrailev and D. L. Shepelyansky, *Dynamical stochasticity in classical*  
936 *and quantum mechanics*, Sov. Scient. Rev. C **2**, 209 (1981).
- 937 [37] D. Shepelyansky, *Ehrenfest time and chaos*, Scholarpedia **15**(9), 55031 (2020),  
938 doi:[10.4249/scholarpedia.55031](https://doi.org/10.4249/scholarpedia.55031).
- 939 [38] A. Lakshminarayan, *Modular multiplication operator and quantized baker's maps*, Phys.  
940 Rev. A **76**(4), 042330 (2007).
- 941 [39] A. M. Patoary, A. Vikram, L. Shou and V. Galitski, *Chaotic roots of the modular multipli-*  
942 *cation dynamical system in Shor's algorithm*, preprint arXiv:2306.16446 .
- 943 [40] F. Leyvraz, C. Schmit and T. H. Seligman, *Anomalous spectral statistics in a symmetrical*  
944 *billiard*, J. Phys. A **29**(22), L575 (1996), doi:[10.1088/0305-4470/29/22/004](https://doi.org/10.1088/0305-4470/29/22/004).
- 945 [41] J. P. Keating and J. M. Robbins, *Discrete symmetries and spectral statistics*, J. Phys. A  
946 **30**(7), L177 (1997), doi:[10.1088/0305-4470/30/7/006](https://doi.org/10.1088/0305-4470/30/7/006).
- 947 [42] B. Gutkin, *Dynamical 'breaking' of time reversal symmetry*, J. Phys. A **40**(31), F761  
948 (2007), doi:[10.1088/1751-8113/40/31/F02](https://doi.org/10.1088/1751-8113/40/31/F02).
- 949 [43] C. Dembowski, H.-D. Gräf, A. Heine, H. Rehfeld, A. Richter and C. Schmit, *Gaussian*  
950 *unitary ensemble statistics in a time-reversal invariant microwave triangular billiard*, Phys.  
951 Rev. E **62**, R4516 (2000), doi:[10.1103/PhysRevE.62.R4516](https://doi.org/10.1103/PhysRevE.62.R4516).
- 952 [44] V. Oganessian and D. A. Huse, *Localization of interacting fermions at high temperature*,  
953 Phys. Rev. B **75**, 155111 (2007), doi:[10.1103/PhysRevB.75.155111](https://doi.org/10.1103/PhysRevB.75.155111).

- 954 [45] N. Rosenzweig and C. E. Porter, “Repulsion of energy levels” in complex atomic spectra,  
955 Physical Review **120**(5), 1698 (1960).
- 956 [46] M. V. Berry and M. Robnik, *Semiclassical level spacings when regular and chaotic orbits*  
957 *coexist*, J. Phys. A: Math. Gen. **17**(12), 2413 (1984).
- 958 [47] U. Smilansky, S. Tomsovic and O. Bohigas, *Spectral fluctuations and transport in phase*  
959 *space*, J. Phys. A **25**(11), 3261 (1992), doi:[10.1088/0305-4470/25/11/029](https://doi.org/10.1088/0305-4470/25/11/029).
- 960 [48] O. Giraud, N. Macé, E. Vernier and F. Alet, *Probing symmetries of quantum*  
961 *many-body systems through gap ratio statistics*, Phys. Rev. X **12**, 011006 (2022),  
962 doi:[10.1103/PhysRevX.12.011006](https://doi.org/10.1103/PhysRevX.12.011006).
- 963 [49] N. L. Balazs and A. Voros, *The quantized baker’s transformation*, Ann. Physics **190**(1), 1  
964 (1989), doi:[10.1209/0295-5075/4/10/001](https://doi.org/10.1209/0295-5075/4/10/001).
- 965 [50] M. Saraceno, *Classical structures in the quantized baker transformation*, Ann. Physics  
966 **199**(1), 37 (1990), doi:[10.1016/0003-4916\(90\)90367-W](https://doi.org/10.1016/0003-4916(90)90367-W).
- 967 [51] E. Ott, *Chaos in dynamical systems*, Cambridge University Press, second edn.,  
968 doi:[10.1017/CBO9780511803260](https://doi.org/10.1017/CBO9780511803260) (2002).
- 969 [52] T. A. Brun and R. Schack, *Realizing the quantum baker’s map on a NMR quantum computer*,  
970 Phys. Rev. A **59**(4), 2649 (1999).
- 971 [53] Y. S. Weinstein, S. Lloyd, J. Emerson and D. G. Cory, *Experimental implemen-*  
972 *tation of the quantum baker’s map*, Phys. Rev. Lett. **89**(15), 157902 (2002),  
973 doi:<https://doi.org/10.1103/PhysRevLett.89.157902>.
- 974 [54] N. Anantharaman and S. Nonnenmacher, *Entropy of semiclassical measures of the Walsh-*  
975 *quantized baker’s map*, Ann. Henri Poincaré **8**(1), 37 (2007), doi:[10.1007/s00023-006-](https://doi.org/10.1007/s00023-006-0299-z)  
976 [0299-z](https://doi.org/10.1007/s00023-006-0299-z).
- 977 [55] T. Eisner, B. Farkas, M. Haase and R. Nagel, *Operator theoretic aspects of ergodic theory*,  
978 vol. 272 of *Graduate Texts in Mathematics*, Springer, Cham, doi:[10.1007/978-3-319-](https://doi.org/10.1007/978-3-319-16898-2)  
979 [16898-2](https://doi.org/10.1007/978-3-319-16898-2) (2015).
- 980 [56] I. P. Cornfeld, S. V. Fomin and Y. G. Sinai, *Ergodic theory*, vol. 245 of *Grundlehren der math-*  
981 *ematischen Wissenschaften [Fundamental Principles of Mathematical Sciences]*, Springer-  
982 Verlag, New York, doi:[10.1007/978-1-4615-6927-5](https://doi.org/10.1007/978-1-4615-6927-5), Translated from the Russian by A.  
983 B. Sosinskiĭ (1982).
- 984 [57] J. G. Sinai, *A weak isomorphism of transformations with invariant measure*, Dokl. Akad.  
985 Nauk SSSR **147**, 797 (1962).
- 986 [58] E. Glasner, *Ergodic theory via joinings*, vol. 101 of *Mathematical Surveys and Monographs*,  
987 American Mathematical Society, Providence, RI, doi:[10.1090/surv/101](https://doi.org/10.1090/surv/101) (2003).
- 988 [59] M. Saraceno and A. Voros, *Towards a semiclassical theory of the quantum baker’s map*,  
989 Phys. D **79**(2-4), 206 (1994), doi:[10.1016/S0167-2789\(05\)80007-7](https://doi.org/10.1016/S0167-2789(05)80007-7).
- 990 [60] S. De Bièvre and M. Degli Esposti, *Egorov theorems and equidistribution of eigenfunctions*  
991 *for the quantized sawtooth and baker maps*, Ann. Inst. H. Poincaré Phys. Théor. **69**(1), 1  
992 (1998).

- 993 [61] Y. Y. Atas, E. Bogomolny, O. Giraud and G. Roux, *Distribution of the ratio of consecu-*  
994 *tive level spacings in random matrix ensembles*, Phys. Rev. Lett. **110**, 084101 (2013),  
995 doi:[10.1103/PhysRevLett.110.084101](https://doi.org/10.1103/PhysRevLett.110.084101).
- 996 [62] P. W. O'Connor and S. Tomsovic, *The unusual nature of the quantum baker's trans-*  
997 *formation*, Ann. Physics **207**(1), 218 (1991), doi:[https://doi.org/10.1016/0003-](https://doi.org/10.1016/0003-4916(91)90184-A)  
998 [4916\(91\)90184-A](https://doi.org/10.1016/0003-4916(91)90184-A).
- 999 [63] A. M. Ozorio de Almeida and M. Saraceno, *Periodic orbit theory for the quantized baker's*  
1000 *map*, Ann. Physics **210**(1), 1 (1991), doi:[10.1016/0003-4916\(91\)90274-C](https://doi.org/10.1016/0003-4916(91)90274-C).
- 1001 [64] D. Burgarth, G. Chiribella, V. Giovannetti, P. Perinotti and K. Yuasa, *Ergodic and mixing*  
1002 *quantum channels in finite dimensions*, New Journal of Physics **15**(7), 073045 (2013).
- 1003 [65] S. Singh, N. Datta and I. Nechita, *Ergodic theory of diagonal orthogonal covariant quantum*  
1004 *channels*, preprint arXiv:2206.01145 (2022).
- 1005 [66] S. Pilatowsky-Cameo, C. B. Dag, W. W. Ho and S. Choi, *Complete Hilbert-space ergodicity*  
1006 *in quantum dynamics of generalized Fibonacci drives*, preprint arXiv:2306.11792 (2023).
- 1007 [67] O. Costin and J. L. Lebowitz, *Gaussian fluctuation in random matrices*, Phys. Rev. Lett.  
1008 **75**(1), 69 (1995).
- 1009 [68] R. Aurich, J. Bolte and F. Steiner, *Universal signatures of quantum chaos*, Phys. Rev. Lett.  
1010 **73**(10), 1356 (1994).
- 1011 [69] R. Aurich, A. Bäcker and F. Steiner, *Mode fluctuations as fingerprints of chaotic and non-*  
1012 *chaotic systems*, Int. J. Mod. Phys. B **11**(07), 805 (1997).
- 1013 [70] T. A. Brody, J. Flores, J. B. French, P. Mello, A. Pandey and S. S. Wong, *Random-matrix*  
1014 *physics: spectrum and strength fluctuations*, Rev. Mod. Phys. **53**(3), 385 (1981).
- 1015 [71] A. Bouzouina and S. De Bièvre, *Equipartition of the eigenfunctions of quantized ergodic*  
1016 *maps on the torus*, Comm. Math. Phys. **178**(1), 83 (1996).
- 1017 [72] M. Degli Esposti, S. Nonnenmacher and B. Winn, *Quantum variance and ergodicity for the*  
1018 *baker's map*, Comm. Math. Phys. **263**(2), 325 (2006), doi:[10.1007/s00220-005-1397-3](https://doi.org/10.1007/s00220-005-1397-3).
- 1019 [73] A. Bäcker, *Numerical aspects of eigenvalue and eigenfunction computations for chaotic*  
1020 *quantum systems*, In *The mathematical aspects of quantum maps*, vol. 618 of *Lecture*  
1021 *Notes in Phys.*, pp. 91–144. Springer, Berlin, ISBN 3-540-02623-1, doi:[10.1007/3-540-](https://doi.org/10.1007/3-540-37045-5_4)  
1022 [37045-5\\_4](https://doi.org/10.1007/3-540-37045-5_4) (2003).